An innovative method for measuring the convective cooling of photovoltaic modules

Baptiste Amiot, Hervé Pabiou, Rémi Le Berre, Stéphanie Giroux-Julien

Solar Energy 274 (2024) 112531

Contents lists available at ScienceDirect

Solar Energy

journal homepage: www.elsevier.com/locate/solener

An innovative method for measuring the convective cooling of photovoltaic modules

Baptiste Amiot [a,d,*], Hervé Pabiou [b], Rémi Le Berre [c], Stéphanie Giroux–Julien [d]

[a] CEREA - Ecole Nationale des Ponts et Chaussees, EDF R&D, Marne la Vallee 77455, France
[b] CNRS, INSA-Lyon, CETHIL, UMR5008, F-69621 Villeurbanne, France
[c] EDF R&D - Dpt. Technology and Research for Energy Efficiency, Ecuelles 77250, France
[d] Universite Claude Bernard Lyon 1, CETHIL, UMR5008, CNRS, INSA Lyon, Villeurbanne F-69100, France

ARTICLE INFO

Keywords:
Convective heat transfer
Experimental
Heat flux sensor
Floating photovoltaics

ABSTRACT

The temperature of photovoltaic (PV) cells is a critical factor in evaluating energy yield and predicting system degradation. Although thermo-electrical models allows predicting the evolution of the system over time, precise understanding of the thermal exchanges between the system and its environment is needed as they are implemented in the yield assessment using thermal correlations. These empirical correlations are based on heat transfer magnitudes undergone by similar PV set-ups.

The aim of this study is to introduce a non-intrusive experimental methodology for precisely determining the convective heat transfer coefficient (CHTC) at the front of photovoltaic modules using two setups. The method integrates a heat flux sensor glued to the PV surface coupled with environmental data (e.g., irradiance, ambient temperature). This experimental method is applied to PV modules on a roof in an urban area and to a floating photovoltaic (FPV) system. It is demonstrated that the method significantly improves the accuracy of prediction of PV module temperatures in operating conditions compared to the conventional method based on the energy balance of a PV module.

By using quantile regression, an empirical forced convection correlation is found based on the average wind speed. Compared to the traditional approach which relies on global transmittance, the CHTC is mainly dependent on the wind, whereas the global transmittance includes the radiative heat transfer which depends on the module temperature. The correlation for CHTC tailored for the floating photovoltaic system shows sensitivity to wind speed that is slightly higher compared to the inland setup in the literature.

1. Introduction

Making an accurate forecast of the energy yield of photovoltaic (PV) systems requires modeling the thermal behavior of PV modules, as temperature has a negative effect on the electrical output of crystalline silicon solar cells ($\simeq 0.4\,\%/K$) [1]. The challenge in predicting temperature arises from the task of assessing the energy balance at the system level which necessitates the description of multiple heat modes with varying magnitudes. It is common practice to directly determine the temperature of the system as a function of environmental conditions [2]. However, this method is rarely reproducible as it assumes how energy transits from the PV system to the environment, so empirical temperature correlations have to be formulated for each PV installation geometry. In their study, Theristis et al. [3] demonstrated that when comparing several PV models used in the solar community, the approximate description of heat exchange leads to a wide range of temperature predictions, with variations of up to 15 °C at $1000\,W\,m^{-2}$. This has a significant impact on energy yield predictions, which can differ by up to 6 %. It is noteworthy that even more sophisticated thermal models, which combine radiative and convective transfer modes into a single thermal coefficient, denoted U_{values} hereafter, must still overcome limitations in their predictions. These limitations arise from the choice of thermal coefficients found in the existing literature. The two paths to improvement are therefore: to offer more options in thermal correlations in the literature, and improve thermal description by using a separate set of coefficients per thermal mode involved. In the study by Driesse et al. [4], dissociating the thermal radiative component from the convective action is shown to improve thermal prediction for a low numerical cost and requires only few data inputs (environment temperature, PV material properties). However, in doing so, the prediction issue is found to be displaced in the accurate description of convective heat transfer, which is still needed to be implemented

* Corresponding author at: CEREA - Ecole Nationale des Ponts et Chaussees, EDF R&D, Marne la Vallee 77455, France.
E-mail address: baptiste.amiot@enpc.fr (B. Amiot).

https://doi.org/10.1016/j.solener.2024.112531
Received 21 December 2023; Received in revised form 5 April 2024; Accepted 7 April 2024
Available online 25 April 2024

Nomenclature

Index notation

m	Module
h	Heat flux sensor
fr	Front module side
re	Rear module side
grd	Ground
amb	Ambient
sky	Sky
gl	Glass
eva	EVA
si	Silicone
b	Black coating
w	White coating
sw	Short-wavelength
lw	Long-wavelength
cd	Conductive heat transfer mode
rad	Radiative heat transfer mode
cv	Convective heat transfer mode
c	Constant parameter in linear function
v	Wind related parameter in linear function

Physical Properties

h	Convective heat rates (CHTC) $\mathrm{W\,K^{-1}\,m^{-2}}$
GTI	Global Tilted Irradiance $\mathrm{W\,m^{-2}}$
GHI	Global Horizontal Irradiance $\mathrm{W\,m^{-2}}$
U_{values}	Thermal transmittance $\mathrm{W\,K^{-1}\,m^{-2}}$
T	Temperature K
$\overline{U}$	Wind velocity $\mathrm{m\,s^{-1}}$
P	Electrical Production $\mathrm{W\,m^{-2}}$
R	Thermal Resistance $\mathrm{K\,W^{-1}}$
C	Thermal Capacitance $\mathrm{J\,K^{-1}}$
ρ	Density $\mathrm{kg\,m^{-3}}$
c_p	Specific Heat Capacity $\mathrm{J\,kg^{-1}\,K^{-1}}$
$\mathcal{L}$	Length m
$\mathcal{A}$	Area $\mathrm{m^2}$
k	Thermal Conductivity $\mathrm{W\,m^{-1}\,K^{-1}}$

Greek Letters

τ	Quantile level
r	Reflectivity
$\alpha_{x,S}$	Absorptivity in spectral range x of surface S
ϕ	Density of flux $\mathrm{W\,m^{-2}}$
$\sigma = 5.67 \times 10^{-8}\ \mathrm{W\,m^2\,K^{-4}}$	Stefan–Boltzmann constant

in thermal models. This heat transfer is classically characterized by the convective heat transfer coefficient (CHTC) which is defined by the ratio of the convective heat flux and the temperature difference between the surface of the module and the surrounding air.

The convective heat transfer on a solar collector is driven by the atmospheric flow, the geometry of the system [5] and the existence of nearby obstructions [6]. Other parameters like flow direction are also found to affect the CHTC [7]. A more pragmatic approach is to depict the CHTC as a function of wind velocity; for instance the study conducted by Test et al. [8], focusing on a 40°-tilted flat plate, yielded the following relation:

$$h_{Te} = \underbrace{8.56}_{h_c} + \underbrace{2.55}_{h_v}\,\overline{U} \tag{1}$$

in which $\overline{U}$ is the mean wind velocity given in $\mathrm{m\,s^{-1}}$ and observed one meter above the solar collector, the CHTC is denoted h ($\mathrm{W\,K^{-1}\,m^{-2}}$). The linear relationship (1) is derived from the widely accepted assumption that a fully turbulent boundary layer develops over the module's surface in the external environment. The linear form of this equation is justified by the limited range of wind speed typically observed around PV systems [$0.8\,\mathrm{m\,s^{-1}}$-$5\,\mathrm{m\,s^{-1}}$] as detailed in Appendix A.1. Due to the turbulent flow hypothesis, the constant parameter h_c does not represent the CHTC in the absence of wind. Notably, empirical evidence suggests that the coefficient h_c exhibits significant variability across different studies, as illustrated by Kumar et al. [9]. This difference is mainly attributed to the level of turbulence in the environment, the constant coefficient increasing with the magnitude of the disturbances. In contrast, the wind dependency component h_v remains relatively stable across various empirical correlations (refer to Figure 5 in [9]).

The utilization of a PV thermal model that includes convective and radiative heat transfer modes with wind dependent CHTCs has proven to be effective in accurately forecasting the temperature of a PV module and its changes over time [10]. Nonetheless, determining the convective parameters h_c and h_v still requires experimental efforts, as no analytical solution exists. Usually, the convective heat transfer is measured using an instrumented plate whose temperature allows obtaining the CHTC by means of an energy balance [11]. However, the thermal inertia of the measurement system's limits and hinders the efficient determination of convective transfer rates over short time scales. To overcome this issue, a solution has been explored in the field of building science. This involves incorporating heat flux sensors into the system, typically within walls. The global transmittance value can then be measured without the need for prior knowledge regarding system properties [12], as long as the sensor does not disturb the heat flow [13]. Additional processing steps are required to eliminate abnormal values, particularly when the temperature difference between walls and the environment is too small [14]. For example, In their study, Albatici et al. [15] utilized a heat flux sensor and an infrared camera to calculate the U_{values} parameter for opaque building components. The heat flux sensor was found to accurately capture the thermal reaction of the wall caused by wind excitation. This makes it a promising option to determine the coefficient of convective heat transfer coefficient h. Additionally, the thinness of the heat flux sensor, which can be as low as 0.5 mm, helps minimize sensor intrusiveness. To the author's knowledge, only the work of Hayakawa et al. [16] has shown the use of heat flux sensors in the domain of photovoltaics. In this study, a vehicle-integrated photovoltaic system is monitored so that the complex fluid/module interactions introduced by vehicle motion combined with local wind make the heat flux sensor technique appropriate for determining the CHTC.

In the context of land scarcity, photovoltaic installations are emerging in new environments such as floating PVs (FPV) and agrivoltaics with considerable potential for development. For example, using a mere 10 % of the surface areas of current hydro-reservoirs for floating solar installations could generate the same amount of electrical energy as traditional fossil fuels [17] with limited land-use impacts. However, the proliferation of FPV can have notable effects on the thermal structure of lakes [18], creating intricate interactions with aquatic ecosystems, while the decision-making process for choosing installation locations continues to primarily depend on lake morphology [19]. Importantly, the temperature of FPV modules has emerged as a crucial factor influencing cost competitiveness [20]. Hence, the limited availability of empirical laws for CHTC poses a challenge for the implementation of photovoltaics in such environments. As a result, temperature forecasts are often distorted by the use of substitute CHTCs (inland or rooftop-based). However, the underlying physical causes of this phenomenon

remain uncertain; in addition to convective and radiative transfers, the role of the free evaporating surface has not been fully elucidated. The work of Tina et al. [21] showed that introducing the evaporation mechanism into an advanced numerical model leads to good temperature predictions; a temperature drop of the order of 4 °C was also measured compared to a roof installation under low wind velocity conditions. However, despite the increasing number of authors demonstrating the modification of evaporation by floating solar power plants [22], and the complex relationship between the reduction in evaporation and the distribution of covered areas in a more general context [23], obtaining full understanding of the role of evaporation in the reduction of temperature remains challenging. In [24], Liu et al. conducted a significant study that emphasized the importance of the parameter known as *footprint* in determining the overall heat transfer rate. The footprint is related to the degree of water coverage by the photovoltaic modules and floats; it is said to be "small" or "large" for a low or high degree of coverage, respectively. The study revealed that the heat transfer efficiency of installations with larger footprints is lower. This suggests an inverse correlation between the size of the footprint and the reduction in temperature. Similarly, Bontempo et al. [25] showed that evaporation from floating photovoltaic power plants follows the same type of relationship, i.e. more coverage implies less evaporation. Other environmental factors are also suspected to participate in the cooling effect of FPV, such as wind regime [26] and climate conditions [27].

Convective cooling remains the main source of uncertainty explaining the *cooling effect*. Indeed, the work of Peters et al. [26] showed unexpected overheating of the FPV with respect to rooftop installations. This observation is explained by the fact that wind speed is lower close to the ground compared to the wind-speed at roof level, which has a significant impact on the CHTC. The authors also associated the presence of obstacles to atmospheric flow with this reduction in the cooling effect. Moreover, cooling effects in FPV systems are probably related to their specific geometry, as suggested by existing wind tunnel experiment for conventional solar power plants [28]. Geometrical attributes like module height above the water-ground [29] or row-spacing [30] change the airflow structure beneath the FPV system [31], and it also has an impact on the large-scale turbulent structure above the PV system [32].

The aim of this work is to showcase a new method that determines convective heat transfer coefficients h more precisely using a heat-flux sensor with an application specific to floating photovoltaic systems. Section 2 introduces the measurement principle and the setup details for two experiments carried out under real conditions in 2022. Both experiments have different objectives, and the results shown in Section 3 are separated into two parts. First, the performance of the proposed measurement technique is demonstrated on a rooftop system where the environmental effects on the heat rates are discussed. Then, the heat rates are determined experimentally for one of the floating modules that was installed on a prototype of FPV system. A detailed thermal model is fed by the convective heat transfer coefficient obtained on both sites in view to demonstrating that the methodology can be implemented in an energy yield assessment tool.

2. Material & method

This section is separated into three topics that describe the methodology of determination (Sections 2.1 and 2.2), the two measurement campaigns (Section 2.3, Section 2.4) and the numerical thermal model implemented in the study (Section 2.5).

2.1. Convective heat transfer coefficient measurement

The measurement protocol relies on a specifically coated heat flux sensor that is glued to the front face of the PV module, as shown in Fig. 1. Three heat flux sensors are involved in the study, two of them are installed on the inland experiment whereas the third is installed on the FPV experimental set up. The sensors are painted to control radiative properties: the two sensors of the inland experiment are painted white and black, and the sensor of the FPV system is painted black. All the sensors are manufactured by Captec® and have a sensitivity around 6 $\mu V/Wm^{-2}$. The heat flux sensors are custom-made (10 mm × 120 mm × 1 mm) to fit between the cells on the front surface of the PV module to avoid cell shading.

Table 1
Radiative properties of the two coatings applied on the heat flux sensors and obtained from the laboratory spectroscopy measurements.

	White painting	Black painting
$\alpha_{sw,\mathrm{h}}$	0,30	0,95
$\alpha_{lw,\mathrm{h}}$	0,51	0,95

The heat flux measured by the sensor is the sum of the net radiative heat flux ϕ_{rad} and the convective heat flux ϕ_{cv}, it reads:

$$\begin{aligned}\phi_{\mathrm{h}} &= \phi_{rad} + \phi_{\mathrm{cv}} \\ &= \phi_{rad} + h_{\mathrm{h}}(T_{\mathrm{h}} - T_{amb})\end{aligned} \tag{2}$$

where h_{h} is the CHTC and T_{amb} is the temperature of the air in the vicinity of the sensor. In fact, the local heat flux above a solar cell is slightly different than the one measured above a busbar region, but this was found to be the best compromise to determine a representative CHTC for the PV module. The 1 mm thickness of the sensor allows considering that the probe is located within the thermal boundary layer that develops on the module surface. Therefore, the CHTC measured by the sensor is assumed to be equal to that over the PV module: $h_{\mathrm{h}} = h_{fr}$. Assuming that the surface of the sensor is gray and isotropic, the net radiative heat flux leaving the sensor can be written as:

$$\phi_{rad} = \alpha_{lw,\mathrm{h}}\sigma T_{\mathrm{h}}^4 - \alpha_{sw,\mathrm{h}}\mathrm{GTI}_{sw} - \alpha_{lw,\mathrm{h}}\mathrm{GTI}_{lw} \tag{3}$$

where $\sigma = 5.67 \times 10^{-8}\ \mathrm{W\,m^{-2}\,K^{-4}}$ is the Stefan–Boltzmann constant, T_{h} is the temperature of the sensor in K, GTI_{sw} and GTI_{lw} are the plane of array irradiances for the short-wavelength and long-wavelength ranges, respectively. Absorptivity in the short-wavelength range $\alpha_{sw,\mathrm{h}}$ and the long wavelength range $\alpha_{lw,\mathrm{h}}$ of the sensor coating is measured by a Fourier Transform Spectrometer with an integrating sphere equipped for infrared and visible ranges. The corresponding radiative properties are shown in Table 1. Details about the spectroscopy results and calculation of the net radiative heat flux are given in Appendix A.2.

Using Eqs. (3) and (2), the CHTC reads:

$$h_{\mathrm{h}} = \frac{\phi_{\mathrm{h}} - \alpha_{lw,\mathrm{h}}\sigma T_{\mathrm{h}}^4 + \alpha_{sw,\mathrm{h}}\mathrm{GTI}_{sw} + \alpha_{lw,\mathrm{h}}\mathrm{GTI}_{lw}}{T_{\mathrm{h}} - T_{amb}} \tag{4}$$

When there is only a small temperature difference $T_{\mathrm{h}} - T_{amb}$, the calculation of the CHTC becomes insignificant. As a result, the calculation of h_{h} does not include cases where $T_{\mathrm{h}} - T_{amb}$ is less than or equal to 4 °C. These conditions are typically observed during nighttime and when there are persistent cloudy conditions.

2.2. Statistical analysis of convective heat transfer

Convective heat transfer coefficients are usually sought as a linear function of wind speed, as explained in Appendix A.1. However, this relationship can be modified by other factors such as wind direction, wind turbulence magnitude, soiling or instrumental disturbances. Therefore, experimental data is subject to considerable dispersion and outliers that can have an impact on the statistical analysis and the estimated coefficients h_c and h_v. To improve the determination of CHTC, we suggest using the quantile regression tool, which makes it possible to obtain more information than the classical root mean square regression. Quantile regression is used in many disciplines where conditional regressions can provide additional understanding of a relation between two

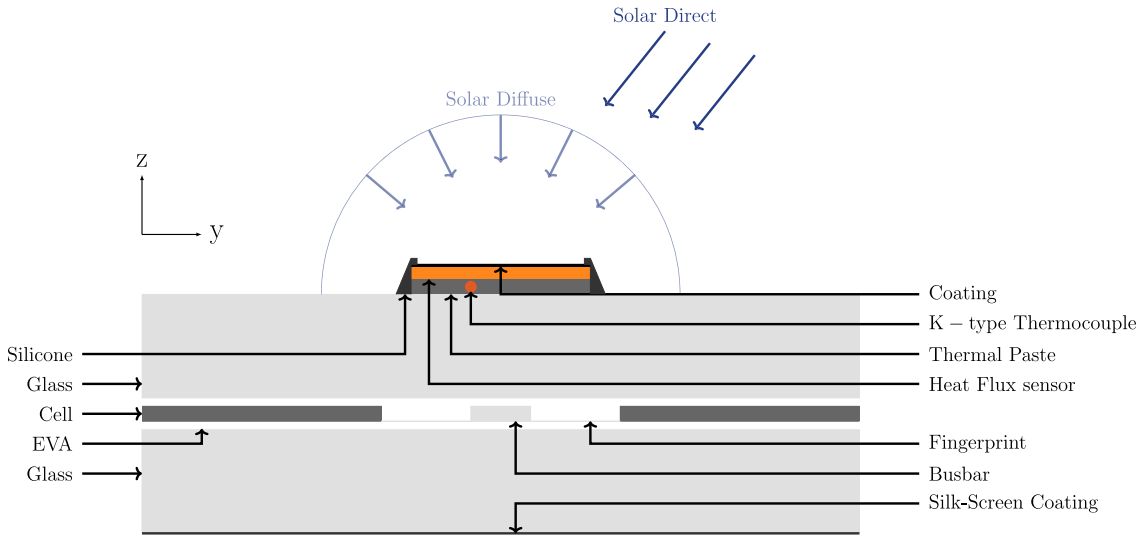

Fig. 1. Transversal view of the heat flux sensor on top of the PV module.

variables [33]. Simple examples of cases of utilization are described in [34], and mainly cover the fields of human-related fields sciences (economics, demography, medicine) and the environment (climate, meteorology, hydrology).

In statistics, quantiles are cut-off points that divide a data set into subsets of equal probability. Let h_τ be the quantile of the CHTC that divides the dataset such that each observation h_i has a probability of τ to be less than h_τ. Thus, $h_{0.5}$ is the median. For a quantile regression, instead of finding the variable of interest (h) as a linear function of wind velocity ($\overline{U}$), we find a linear regression for each quantile $h_\tau = h_{v,\tau}\overline{U} + h_{c,\tau}$. The coefficients $(h_{v,\tau}, h_{c,\tau})$ are obtained by minimizing the function:

$$E = \sum_{i=1}^{N} \tau \left[h_i - (h_{v,\tau}\overline{U} + h_{c,\tau})\right]_+ + (1-\tau)\left[h_{v,\tau}\overline{U} + h_{c,\tau} - h_i\right]_+ \quad (5)$$

where N is the total number of observations $\left(h_i, \overline{U}_i\right)$, $[X]_+$ is the positive value of X : $[X]_+ = 0.5(X + |X|)$. Whereas the classical least mean square method minimizes the square of the residual, quantile regression minimizes a weighted absolute value of the residual, so that the influence of outliers is reduced. In this work, the function E is computed using the iteratively reweighted least squares algorithm [35]. Three regressions are selected in the analysis: median regression ($\tau = 0.5$) for the best linear estimate of $h = f(\overline{U})$, $\tau = 0.25$ and $\tau = 0.75$ that are referred to as 1st quartile regression and 3rd quartile regression hereafter.

A measure of the spread of experimental CHTC is determined by computing a dispersion indicator, $\Delta(h)$, which is defined as the area between the third and first quartiles in the plane $(h, \overline{U})$ and restricting the wind velocity to the relevant range $0.3 \leq \overline{U} \leq 3$ m s^{-1}. Fig. 2 illustrates the use of the dispersion indicator for a fictitious dataset. The dispersion indicator equal to the area of the orange zone is a measure of the dispersion. This indicator has the advantage of being less sensitive to outliers than the classical standard deviation value.

2.3. Laboratory solar platform

The first dataset comes from an experiment, called Laboratory Solar Platform, that was set up to explore the thermal behavior of photovoltaic modules in an urban environment. Twelve east–west pitched

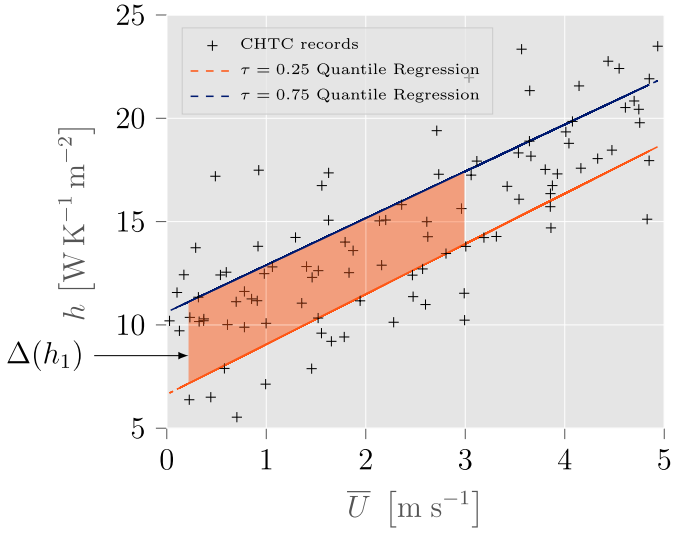

Fig. 2. Illustration of the use of quantile regressions to estimate CHTC dispersion. The dispersion indicator (Δh) is the filled orange surface between the two quartile regressions $\tau = 0.25$ and $\tau = 0.75$.

modules (Photowatt® PW60HT-C-XF) are mounted in portrait mode at a fixed tilt angle of 12° on the roof of the laboratory building near Lyon in France (GPS location: 45.8°N, 4.9°E). They are spread in two groups separated by one meter and composed of six modules each (Fig. 3). The height of the modules from the lower tip with respect to the platform is around 1 m so that few obstacles are located in the vicinity of the installation. The main features of these modules are: half cell technology, glass/glass systems (2 mm per layer), silk screen coating on the rear side. The study places emphasis on one specific module facing east, denoted module of interest hereafter. Detailed performances of the module characteristics were determined in the laboratory and are summarized in Table 2.

Table 3 summarizes the instruments available on the platform. First, the pyranometer (Kipp–Zonen SMP10) and the pyrgeometer (Kipp–Zonen CGR4) are installed at the edge of the installation in the plane

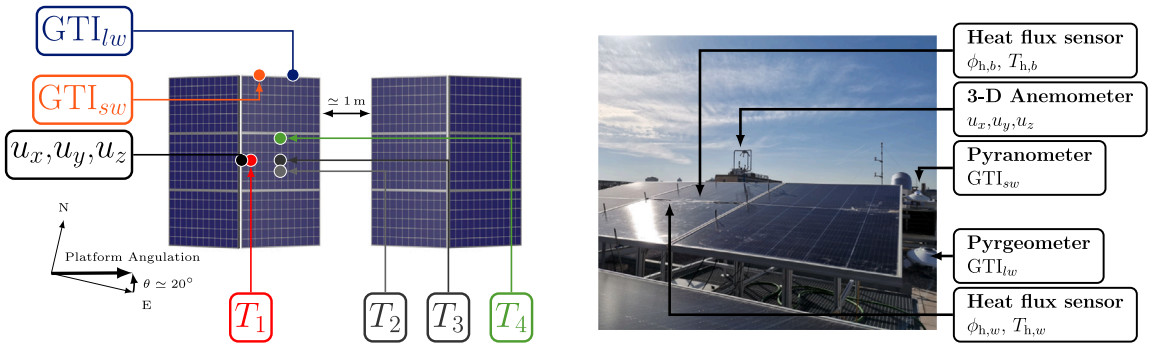

(a) *Diagram of the sensors set and their distribution over the platform.*

(b) *Picture of the module of interest and associated probes.*

Fig. 3. Illustration and picture of the solar platform installed over the laboratory rooftops. The temperature sensors indicated on the left figure are placed on the rear side of the module.

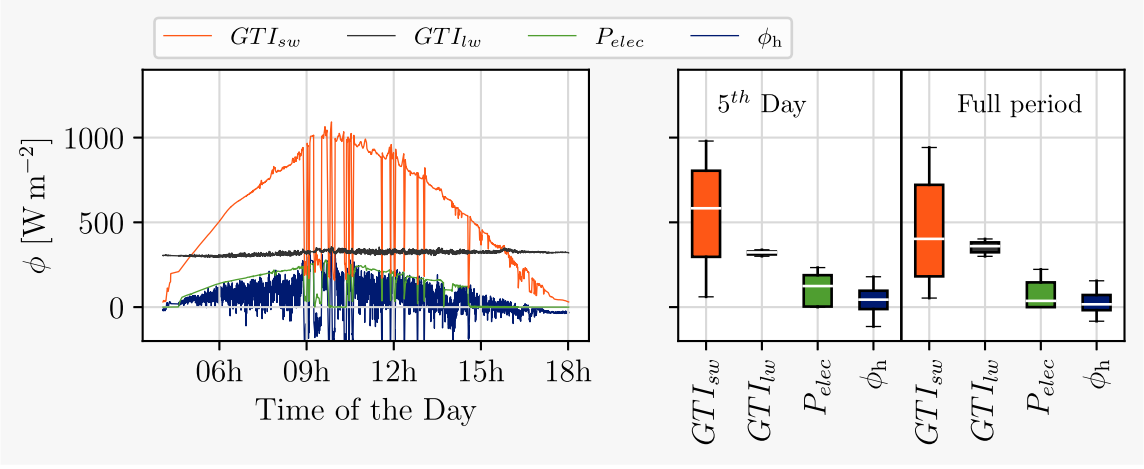

Fig. 4. (left) Time series for the 5th day of the measurement campaign. **(right)** Statistical distribution of measurements for the 5th day of the measurement campaign and the full period of measurements.

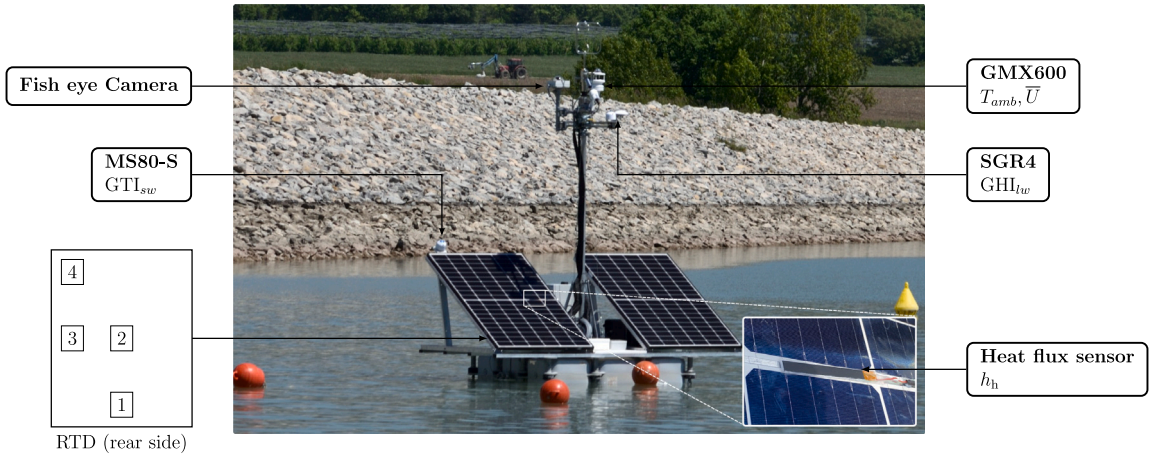

Fig. 5. Position of the sensors in the floating measurement campaign. The heat flux sensor is sealed on the front face of the western module according to the protocol established in Section 2.1.

of the array facing the east side. The panel of interest is equipped with two heat flux sensors with black and white coatings, as described in Section 2.1. In addition, four thermocouples are fixed on the rear side of the module of interest with aluminum tape. We define the spatially averaged temperature on the rear side as: $\langle T \rangle_m = \frac{1}{4}\sum_{i=1}^{i=4} T_i$, and it is used to describe the PV system operating condition. A 3-D anemometer (GILL WindMaster Pro) is set at almost 300 mm of the top edge, it casts a light shade over the module during the afternoon, but its effect is negligible due to the limited footprint of the shadow and to the half-cell technology. Note that only the norm of the velocity vector is used for the study; it is denoted $\overline{U}$ hereafter. The module, connected to a programmable electronic device, works at the maximum power

Table 2
Characteristics of the module under investigation.

I_{SC} [A]	V_{OC} [V]	I_{mpp} [A]	V_{mpp} [V]	FF
9.6	39.2	9.0	32.4	0.75

setting thanks to the incremental conductance algorithm. The eleven other modules work in open-circuit configuration. The air temperature is retrieved using a thermocouple located below the module system and kept away from the sun beam and the influence of the modules. All these sensors are connected to controllers that recover the samples every 5 s for all the probes. The data are then sent to a local server through a wired Ethernet connection.

The first measurement campaign was conducted for sixteen days from May 21st to June 6th 2022. Among the 276 480 records obtained during the period, 103 439 records are above the temperature threshold of 4 °C (Section 2.1) and can be used for the CHTC analysis. Fig. 4 (left) shows changes over time for the short and long-wave downward radiations, the heat flux sensor, and module power production for a typical day. The median value of 16.55 $W^2\,m^{-1}$ for the heat flux at the surface of the module is positive, as expected, since it corresponds to a module that is warmer than the ambient air. The 5 s acquisition captures the fast changes in short-wave radiation corresponding to cloudy spells which lead to sudden drops in electrical power. Fig. 4 (right) shows the distribution of the records for the typical day with respect to the entire dataset. A quick comparison between the distributions shows that the typical day is a good candidate for representing the average behavior of the PV module and environmental conditions.

2.4. Floating measurement campaign

A second observational study was set-up to determine the relationship between CHTC and wind velocity for a floating PV system. A custom-made raft was constructed and equipped with a meteorological mast, two 30°-tilted PV modules and two electrical batteries. The raft was positioned close to an FPV powerplant of around 200 000 m^2 in the south of France. A heat flux sensor painted black was glued to the front surface of the module located on the left of the raft. This module is called module of interest hereafter.

The raft was moored to four gravity anchoring systems so that it remained in place when water levels were high. Although it is possible to reduce yawing motion by positioning the modules and electrical charges with respect to the mass gravity center, it was not possible to fully control the position of the raft during low tides when the hydroelectric power station pumped water. Therefore, the south azimuthal angle of the module of interest could change from time to time.

The environmental conditions were captured using a pyranometer (EKO MS-80S), an integrated weather station (GILL GMX600) and a pyrgeometer (Kipp–Zonen SGR4). The notation of the observed variables is summarized in Table 4. Only the pyranometer was located at the level of the module of interest and positioned in the plane of array, the other probes were located on the mast using deported arms. The PV system was monitored using four RTD sensors displayed over the rear face of the module of interest, as shown in Fig. 5, and the temperature of module operation is determined based on the spatially averaged temperature $\langle T \rangle_m$ using these probes. In fact, the difference in temperatures between sensors can reach several degrees, this is a classical behavior for a standalone configuration as shown in [36]. Spatial averaging allows to reduce uncertainty caused by unavoidable non-uniformity. The heat flux sensor was installed according to the protocol given in Section 2.1. A camera with a fisheye lens was installed on the mast to take a snapshot of the sky every 10 s, and it is used only for the qualitative assessment hereafter.

All the sensors, except the camera, were connected to a NetDL datalogger that recorded data on a minute basis and sent them on a daily basis through GSM. This acquisition loop was connected to the electrical batteries dimensioned to work in standalone mode (*i.e.,* without PV production) for three days. The power required by the sensor set was low; however, night-time periods dried the charge because there was no electrical feed through the PV modules. Although the charge level was not monitored, it was assumed that PV modules work under nominal conditions during the morning to charge the batteries. In the afternoon, the module of interest was assumed to provide very little power to supply all the sensors because of the high charge level of the batteries.

The campaign took place between May and June 2022 for a period of 24 consecutive days. Fig. 6 (left) shows the daily evolution of heat flux sensor flux, as well as the level of short and long wavelength radiations for the 21st day of the campaign. This day was selected because of the changing conditions that occurred around 13:00 that allow contrasting the performance of the measured CHTC values. Fig. 6 (right) indicate the statistical numbers of the data for this precise day and the full dataset. To reduce the influence of non-representative measurements due to mast shadows or changing electrical conditions, the raw data were pre-processed based on timestamps. Only data ranging from 12:00 to 18:00 were kept in the analysis and therefore the dataset contained 9025 data. Note that the statistical values indicated in Fig. 6 (right) are given in this respect. The level of availability was significantly high for all the probes > 99% except for the ambient temperature probe that obtained an availability level of ≃ 93 %. Considering the temperature threshold set used to determine robust CHTC values (see Section 2.1), the usable dataset was reduced to 8196 data.

Fig. 7 shows an overview of the sky cover for five snapshots during the day 21st. These pictures clearly show that the horizon is fairly clear: only a small area of the picture shows the line of the mountain ridge in the north-east, as shown in Fig. 6 (right). These two figures also show that the decrease in cloud density between 12:00 and 16:00 (snapshots 1–4) results in an increase in shortwave radiation and that the largest variations in solar radiation are due to cloud spells. In addition, it can be observed that the short-wavelength fluctuation is not negligible in the late afternoon, whereas the fisheye camera shows a bright sun condition. This is explained by the combination of wind and low-tide effects that made the raft move on the z axis. Installing the pyranometer, the heat flux sensor, and the module in the same frame allowed us to keep these data in the analysis as they moved together accordingly.

2.5. Heat transfer assessment modelings

Two numerical models were built with two distinct objectives: an isothermal model based on the energy balance of a PV module and a multi-layer model which is a more advanced thermal modeling tool used to test the reliability of our heat-flux sensor method. The isothermal method was used to compare the heat flux sensor technique to a conventional method. The multi-layer model took the measured CHTC h_{fr} as an input and reliability was tested by comparing the temperature at the rear side, denoted T_{re}, obtained by the modeling to the measurement. Several CHTCs were tested as an input of the multi-layer model: h_{h} from Eq. (4), the best linear fit using the median regression and denoted $h_{\mathrm{h},0.5}$, h_{Te} from Eq. (1). Radiative fluxes GTI_{sw} and GTI_{lw} and ambient T_{amb} measured by the sensor sets introduced in Sections 2.3 and 2.4 were introduced in the numerical models as boundary conditions.

The isothermal model is an attempt to improve the global thermal transmittance, represented by U_{values}, from the classic Faiman model discussed in [37]. It is expressed as follows:

$$\mathrm{U}_{values} = \frac{\alpha_{sw,m}\mathrm{GTI}_{sw} - \frac{\mathrm{P}_{elec}}{\mathcal{A}}}{T_m - T_{amb}} \tag{6}$$

where $\alpha_{sw,m} = 0.9$ is the absorptivity in the short wavelength range on the front side (including the transmittance of the glass and EVA layers

Table 3
Set of probes installed on the laboratory rooftop and employed in the measurement campaign.

Location	Instrument	Parameters	Timestep (s)	Spectral range (nm)
Side PV module	SMP10	GTI_{sw}	5	285–2800
	SGR4	GTI_{lw}	5	4500–42000
PV module	3-D Anemometer	$u_x\ u_y\ u_z$	5	–
	Heat flux sensor	$\phi_{h,b}$, $\phi_{h,w}$	5	–
	Thermocouple	$T_{h,b}$, $T_{h,w}$, $T_{1\to4}$	5	–

Table 4
Set of probes implemented in the measurement campaign.

Location	Instrument	Parameters	Timestep (s)	Spectral range (nm)
Mast	GMX600	$\overline{U}$, T_{amb}	60	–
	SGR4	GHI_{lw}	60	4500 – 42000
	Fisheye	–	10	–
PV module	MS-80S	GTI_{sw}	60	285 – 3000
	Heat flux sensor	ϕ_h	60	–
	RTD	$T_{1\to4}$	60	–

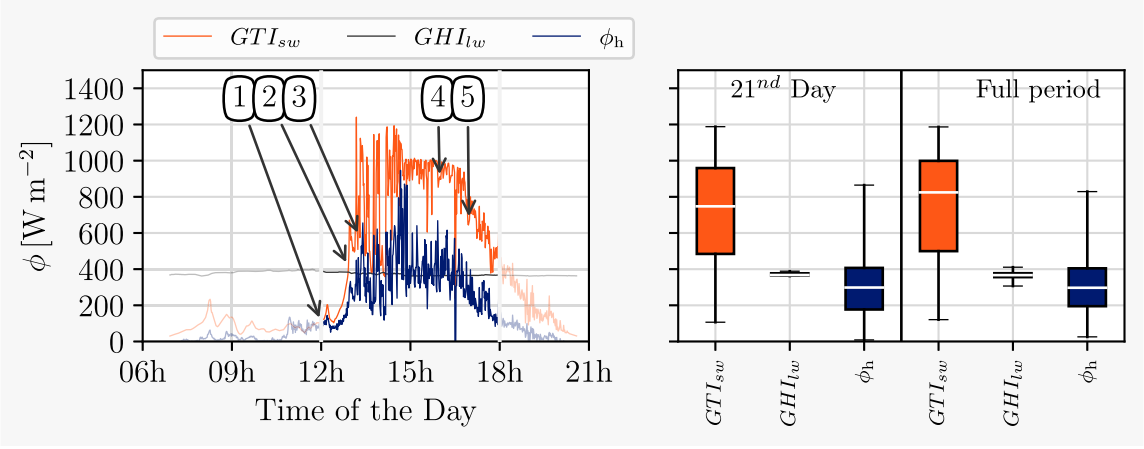

Fig. 6. (left) Time series for the 21st day of the measurement campaign, camera snapshots are indicated in Fig. 7. Only the data ranging from 12:00 and 18:00 were used for the data processing stage. **(right)** Statistical distribution for the 21st day of the measurement campaign and the for the total period. Only timestamps ranging from 12:00 to 18:00 are considered.

Fig. 7. Snapshot of the sky on the 21st day of offshore campaign. The pictures were taken chronologically throughout the day as follows: **(1)** 12:00 cloudy sky; **(2)** 12:55 cloudy sky; **(3)** 13:18 cloudy passages; **(4)** 15:59 clear sky; **(5)** 16:58 clear sky.

and the absorptivity of the silicon), P_{elec} is the electrical power produced by the module and $\mathcal{A}$ is the module surface. The Faiman model is derived from an energy balance in steady state of the PV module where T_m is the average temperature of the module. The isothermal model goes further than the original model by decomposing the overall transmittance value into its radiative and convective components. Assuming steady-state and assuming that the module temperature is equal to the temperature on the rear side ($T_m = T_{re}$), the energy balance of the PV module reads:

$$h_{fr}(T_m - T_{amb}) + \alpha_{lw,m,fr}\left[\sigma T_m^4 - \mathrm{GTI}_{lw}\right] +$$
$$h_{re}(T_m - T_{amb}) + \alpha_{lw,m,re}\sigma\left[T_m^4 - T_{amb}^4\right] = \alpha_{sw,m}\mathrm{GTI}_{sw} - \frac{\mathsf{P}_{elec}}{\mathcal{A}} \quad (7)$$

where h_{re} is the CHTC on the rear side, $\alpha_{lw,m,fr} = \alpha_{lw,m,re} = 0.96$ are the emissivities in the long wave range on the front and rear sides. In Eq. (7), the tilt of the module is neglected, so the view factors are set to one, and the ground is assumed to be a blackbody at temperature T_{amb}. At the rear, natural convection is assumed and h_{re} is modeled by the empirical law from [38]. Indeed, it is more challenging to model heat transfer at the back than at the front, as the airflow is significantly disrupted by the panel, making heat transfer dissimilar to the configuration of forced convection along a flat plate. To address the lack of knowledge of heat transfer in the rear, natural convection is assumed, and its effect is discussed further on. The CHTC produced by the isothermal model is called h_{1d}.

The multilayer model takes the simulation of the temperature field in the module to a higher level of complexity by considering both unsteadiness and spatial heterogeneity. It is created using the Modelica language and the OpenModelica environment. Fundamentally, each layer of the photovoltaic module is reproduced numerically from the thermal standpoint using thermal resistances R and capacities C following the thermal circuit shown in Fig. 8. Module layers are separated

Table 5
Properties of materials implemented in the thermal circuit retrieved from [10]. The glass thickness was adapted from the module specifications sheet.

Material	Thickness [m]	Density [kg m^{-3}]	Conductivity [W m^{-1} K^{-1}]	Specific heat capacity [J kg^{-1} K^{-1}]	Thermal mass [J m^{-2} K^{-1}]
Glass	2×10^{-3}	3×10^{3}	1.8	5×10^{2}	4.5×10^{3}
EVA	3.65×10^{-4}	9.6×10^{2}	3.5×10^{-1}	2.09×10^{3}	7.32×10^{3}
Silicon	1.7×10^{-4}	2.33×10^{3}	1.48×10^{2}	6.7×10^{2}	2.68×10^{2}

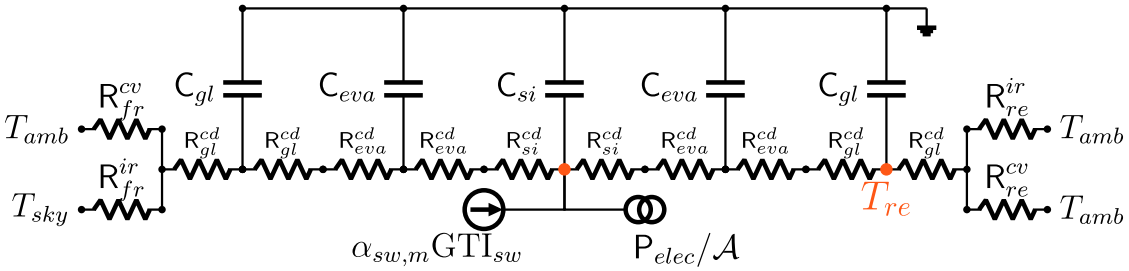

Fig. 8. Multilayer electro-thermal model for the PV module.

into two equal pieces to implement the thermal capacities which read $\mathsf{C} = \rho\mathcal{L}\mathcal{A}c_p$ where ρ, $\mathcal{L}$, $\mathcal{A}$ and c_p are the density, thickness, area, and specific heat capacity of a layer, respectively. Each halved layer is fully conductive and the associated thermal resistance reads $\mathsf{R}^{cd} = \frac{\mathcal{L}}{2k\mathcal{A}}$ in which k is the thermal conductivity. The selected values for the computation are indicated in Table 5. Absorbed visible radiation is implemented at the silicon cell layer as a heat source ($\alpha_{sw,m} = 0.9$) whereas the energy yield is also removed from the budget at this stage. Note that an external Modelica library was used to compute P_{elec}, simulating the electrical part by a single diode approach [39].

On the rear side of the panel, convective R^{cv} and radiative R^{ir} resistances are implemented as:

$$\mathsf{R}^{cv}_{re} = \frac{1}{h_{re}\mathcal{A}} \tag{8}$$

$$\mathsf{R}^{ir}_{re} = \left[\alpha_{lw,m,re}\sigma\mathcal{A}\left(T_{re}+T_{amb}\right)\left(T^2_{re}+T^2_{amb}\right)\right]^{-1} \tag{9}$$

with $\alpha_{lw,m,re} = 0.96$. The rear CHTC is modeled by the empirical law of [38] to mimic a fully natural convective transfer. On the front side, similar expressions hold:

$$\mathsf{R}^{cv}_{fr} = \frac{1}{h_{fr}\mathcal{A}} \tag{10}$$

$$\mathsf{R}^{ir}_{fr} = \left[\alpha_{lw,m,fr}\sigma\mathcal{A}\left(T_{re}+T_{sky}\right)\left(T^2_{re}+T^2_{sky}\right)\right]^{-1} \tag{11}$$

where $\alpha_{lw,m,fr} = 0.96$ and T_{sky} is the sky temperature obtained from the downward long-wavelength radiation $\mathrm{GTI}_{lw} = \sigma T^4_{sky}$. The influence of the form factors on both module faces is minimal due to the low tilt angles in our experiments; they are set to one in this respect.

Two statistical metrics are used to assess the accuracy of the multilayer model, namely the mean bias error (MBE) and the root mean squared error (RMSE), and they read:

$$MBE(X,Y) = \frac{1}{N}\times\sum_{i=1}^{N}\left(X_i - Y_i\right) \tag{12}$$

$$RMSE(X,Y) = \left[\frac{1}{N}\times\sum_{i=1}^{N}\left(X_i - Y_i\right)^2\right]^{1/2} \tag{13}$$

where X and Y are the predicted and experimental temperatures at the rear side, respectively.

3. Results and discussion

The results presented stem from the analysis of the measurements collected from the Laboratory Solar Platform (Sections 3.1–3.4) and from the FPV prototype (Sections 3.5–3.6).

3.1. Influence of sensors on heat transfer

The experimental methodology was designed to minimize intrusiveness on PV module operation. Unflushed probes can have two main effects: decreased electrical production and changes in the module's thermal performance. In order to identify the potential heterogeneity of the temperature of the module, Fig. 9 (left) shows the temperature of the black and white sensors, the four temperatures measured at the back of the module and their averaged value (Fig. 5) during a typical cloudy passage.

The temperatures of the heat flux sensors were in line with the average temperature of the rear face of the module, especially during periods of heating and cooling. However, there was a slight variation in temperature magnitude at local extreme points. For example, during temperature peaks, the black heat flux sensor was generally warmer than the PV module, while the white heat flux sensor was cooler. These temperature variations were expected and stemmed from the greater absorptivity in the short-wavelength spectrum of the black heat flux sensor compared with the module and the white heat flux sensor. The computation of the CHTCs was not influenced because, in forced convection, the CHTC was independent of the temperature of the surface. Importantly, the small hotspot that appears due to the absorptivity of the black heat flux sensor had no noticeable repercussion on the T3 probe, which was closest to the heat flux sensor.

As the thermal capacitance of the sensor was low, varying solar radiations led to rapid probe heating or cooling. Thus, the temperature of the probe behaved differently from the module temperature for short periods (around 10 s). For longer time-scales, the temperature evolution of the black heat flux probes followed the temperature evolution of the module. This temperature variation over a short time-scale had no observable impact on the module temperature so that it did not bias the thermal behavior of the PV module or the determination of the CHTC.

By expanding the observation for the whole measurement campaign in Fig. 9 (right), the median temperatures are found similar for each sensor; they read: $\mathrm{med}\left(T_{\mathrm{h},b}\right) = 35.6\,^{\circ}\mathrm{C}$, $\mathrm{med}\left(T_{\mathrm{h},w}\right) = 34.7\,^{\circ}\mathrm{C}$ and $\mathrm{med}\left(\langle T\rangle_m\right) = 34.2\,^{\circ}\mathrm{C}$. The same observation is made regarding the 1st and 3rd quartiles, it is concluded that temperatures evolved comparably between all the probes. Recalling that $\langle T\rangle_m$ is measured on the rear side and T_{h} is measured on the front side, the small differences in the median temperature are consistent with the work of Weiss et al. [40] showing a typical temperature difference across the module of less than 2 K. This suggests that the heat flux sensors are properly connected to the surface.

When the tails of the distribution are examined, it is evident that the black-coated heat flux sensor underwent temperature variations

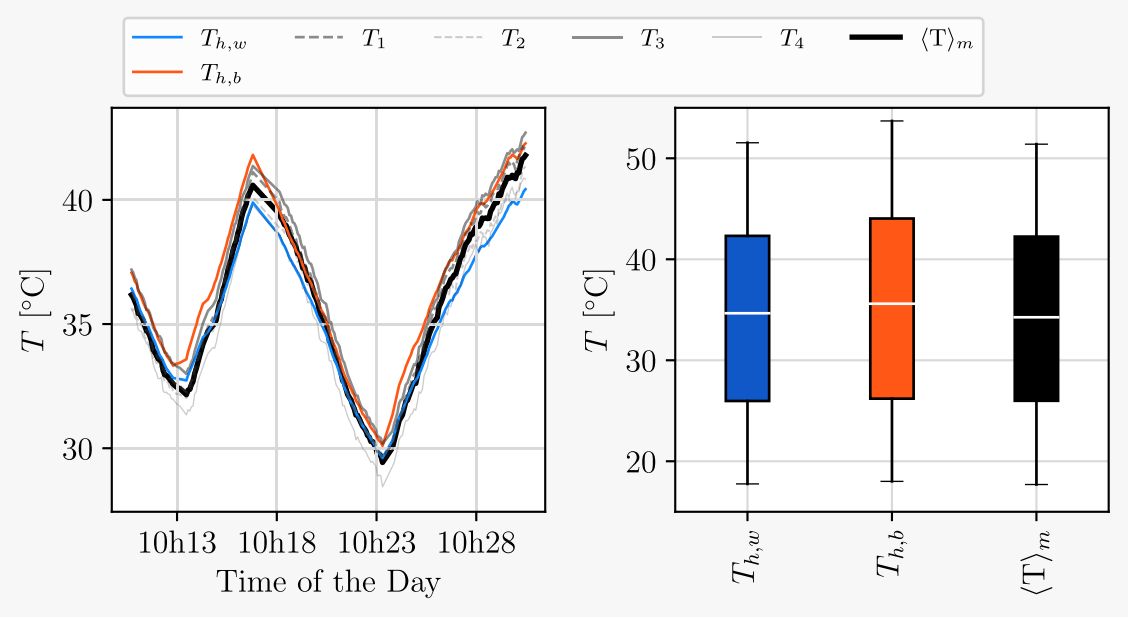

Fig. 9. Temperature measurements for the black and white-coated heat flux sensor, and the module rear side. **(left)** Temperature time series for 30 min during the 5th day of the measurement campaign. **(right)** Temperature statistics for the whole period of the measurement campaign. The horizontal bar within the body of the distribution indicates the median values. The whisker values are calculated at the 5% and 95% points of the distribution, and no outliers are shown.

larger than those of the PV module and the white-coated probe. The variation was mainly due to the greater magnitude of the temperature during periods of high temperature, as depicted by the increase in the upper whisker of the black-coated distribution. The low value observed for the upper whisker of the white coated sensor can be attributed to the lower emissivity with respect to the black coating. Looking at the lower part of the distribution, lower temperature magnitudes are well correlated between all the probe locations, and only slight variations of temperature levels were identified for the white-coated heat flux sensor. The difference remains below 0.4 °C and it was assumed that the lower emissivity of this coating was responsible for this difference.

From these observations, there was no significant influence from the heat flux sensors on the thermal behavior of the PV module. On the spatial scale, the heat flux sensors did not modify the temperature of the PV module and no significant effects from local heating or cooling processes were experienced. On the temporal scale, the heat flux sensors monitored the temperature of the PV module throughout the measurement campaign, except for the short time-scale. The influence of the probe could possibly be further reduced by enhancing the coating properties of the probe to match those of the upper glass of photovoltaic panels. However, as the variation of the spectral emissivity of the white paint was not compatible with a gray approximation on the short- and long-wavelength ranges, only measurements from the black sensor are considered in what follows.

3.2. Convective heat transfer coefficient as a function of wind speed

Convective heat exchange on the module surface is mainly dependent on wind speed, and CHTC is expected to vary linearly with the intensity of the wind Appendix A.1. Fig. 10(a) shows the distribution of the experimental CHTC, calculated using Eq. (4), as a function of the mean wind velocity. Three particular quantile regressions are also indicated ($\tau = 0.25$, $\tau = 0.50$, $\tau = 0.75$), which correspond to the quartile regressions of the dataset.

At first glance, the scattering of the experimental plot appears to be greater for low velocities, but this is a bias associated with the number of points. In fact, in this dataset, the number of points associated with a velocity lower than 2 m s^{-1} is much higher than the number of points associated with high velocities. Therefore, the probability of observing very large (or very low) CHTC values is higher for low velocities. Therefore, the observed scatter is related to the prevalence of low velocity points. This is further evidenced by the fact that the quantile regressions are mostly parallel, indicating that the wind speed affects the mean value of the CHTC rather than its dispersion.

An interesting observation is that the linear relation $h_{\mathrm{h},0.5} = 2.3\overline{U} + 17.93$ has a greater magnitude than that of Eq. (1), which is commonly used in photovoltaic applications in urban areas. This difference is mainly due to the constant term, which depends on the level of turbulence in the natural environment (see Section 1). To obtain Eq. (1), Test et al. added baffles to each side of the heated plate to limit the 3D disturbance, which reduces the disturbance compared to a plate without baffles. Regarding the wind dependency component, it was slightly higher by 10% in Test's experiment, which could be attributed to the inclination of the panel (40° for Test et al. 12° for this study). The wind dependent component h_v was also found to be similar to those obtained in similar configurations, as in [9,10]. The constant component h_c shows different magnitude that can be attributed to the specific environment in which the installation stood, as explained in Section 1.

For comparison, the CHTC obtained by using the isothermal model (Eq. (7)), shown in Fig. 10(b), was found to be lower than the CHTC obtained from the heat flux sensor, and the wind dependency coefficient appeared to be lower. By examining the various terms in Eq. (7), we can see that the main difference between the measurement (h_{h}) and the isothermal model (h_{1d}) comes from the modeling of natural convection at the rear of the module, which tends to modify the heat transfer at the front. With this model, the CHTC at the back depends on the temperature difference between the module and the air, which in turn decreases with wind speed.

From these observations, it appears that the determination of convective heat rates using isothermal modeling is dependent on the heat transfer at the back of the module, for which there is no commonly accepted law. Indeed, the determination of the heat transfer at the back of the module is highly dependent on the geometric configuration of the PV module array and requires specific studies. Considering that the heat flux sensor method does not require inferring the heat transfer occurring over the rear module surface, the CHTC obtained is assessed to be more reliable in determining the front-side heat rate. It also

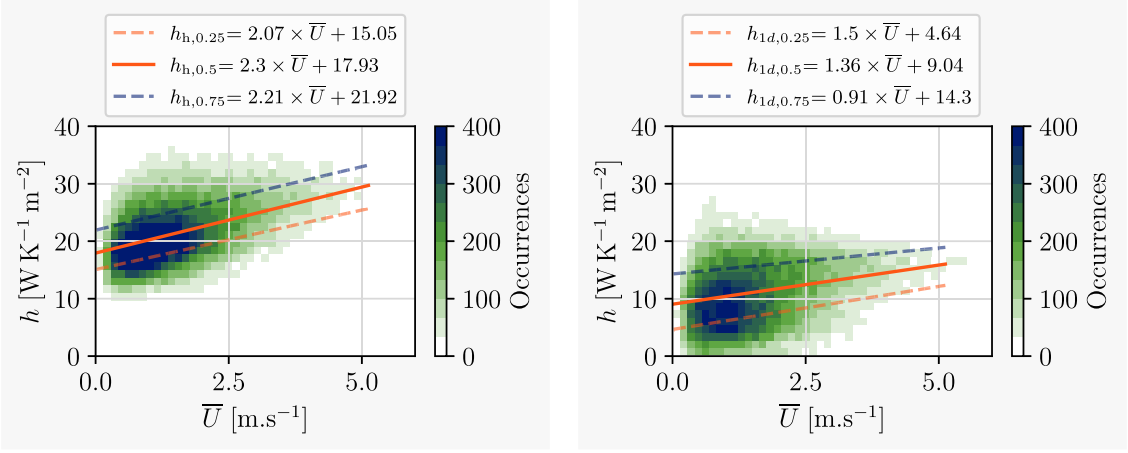

(a) *Measurements* (b) *Isothermal model*

Fig. 10. Convective heat transfer coefficients h obtained by heat flux sensor (a) and computed from isothermal modeling (b) for the laboratory solar platform. The line corresponds to quartile regressions ($\tau = 0.25$, $\tau = 0.50$ and $\tau = 0.75$). Colors indicate the density of records in a given scatter tile.

improves the accuracy of the determination by reducing the dispersion of data, as will be shown in the next section.

Extending the statistical analysis to all quantile regressions, Fig. 11 shows the wind dependency parameter h_v as a function of the quantile order $\tau \in [0, 1]$ for the experimental data ($h_{v,\mathrm{h}}(\tau)$) and for the isothermal model ($h_{v,1d}(\tau)$). Classical linear regressions obtained from root-mean squared minimization are also indicated as constant throughout the range of quantiles. It can be seen that the wind dependency parameter is almost independent on the quantile for the experimental data in the range $0.2 \leq \tau \leq 0.8$ which confirms the observations made on Fig. 10(a): the mean wind speed influences only the mean value of the CHTC and not the scatter. On the contrary, the isothermal model shows a dependence that becomes very considerable for higher quantiles ($\tau \geq 0.5$). This behavior is probably related to the dispersion added by the back natural convection model, which limits the use of such modeling to determine an accurate CHTC. Indeed, both methods lead to the same slope in the smallest quantiles ($\tau \simeq 0.15$), where natural convection at the backside probably leads to a CHTC compatible with the real value.

It is noteworthy that the 95% confidence interval shown in Fig. 11 assesses the quality of the regression regarding the number and distribution of the points, assuming the measurements and the modeling are correct. It cannot be used to assess the quality of the measurement and the model.

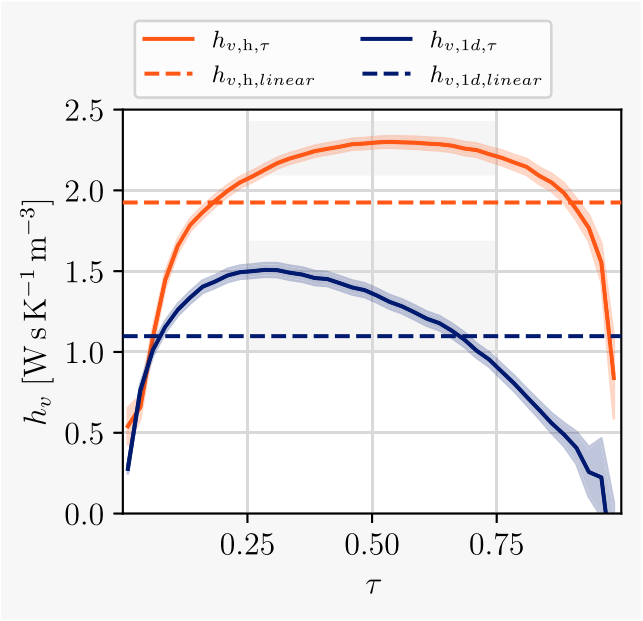

Fig. 11. Slope of the linear quantile regression obtained from experimental data and isothermal model. The colored areas are the confidence intervals 95%. Horizontal dotted lines are the coefficient from a classical regression based on a root-mean square algorithm (rmsa).

3.3. Sensitivities of the dataset to solar radiation and filtering time

One way to analyze the quality of the linear relationship between the CHTC and the wind speed is to compute the regression under a conditional statement (*e.g.,* irradiation higher than 500 W m^{-2}). Fig. 12 shows the dispersion index Δ for the dataset from the laboratory campaign. Three typical conditional statements are investigated because they are likely to influence the CHTC determination methods: irradiation thresholds, irradiation fluctuations, and the filtering time of the data. Fig. 12(a) first shows the dispersion indicator for the irradiance thresholds indicated on the x-axis. These thresholds range between 30 W m^{-2}, where almost all values are included, to 1000 W m^{-2} where only records associated with a higher level are considered. The heat-flux sensor method yields a lower index than that of the isothermal method, suggesting a lower dispersion of the CHTCs for all irradiation levels. For both curves, the dispersion index appears to be almost constant for thresholds below 600 W m^{-2} so that CHTC distribution is not altered. In other words, suppressing the cloudiest days from the analysis does not modify the initial distribution of records. Indeed, the magnitudes of the CHTCs associated with these typical conditions are distributed over the whole range of CHTCs since the heat flux and the temperature difference between the module and the air undergo large fluctuations. As a result, eliminating these days from the dataset does not modify the dispersion index since it tends to eliminate points over the whole range of CHTC values. Above 600 W m^{-2}, the two curves exhibit an increase that is much more pronounced for isothermal modeling. The sharp increase in the dispersion index of the isothermal model for the highest solar radiation conditions could be due to the use of natural convection cooling at the rear of the module. Indeed, a lack of heat transfer at the rear is offset by an increase in heat transfer at the front, as explained in the previous section.

The short-term fluctuations of solar radiation can also influence the dispersion of records because other thermal mechanisms like thermal inertia may pollute CHTC determination. Therefore, the genuine dataset is 10 min-aggregated and each timestamp is associated with the

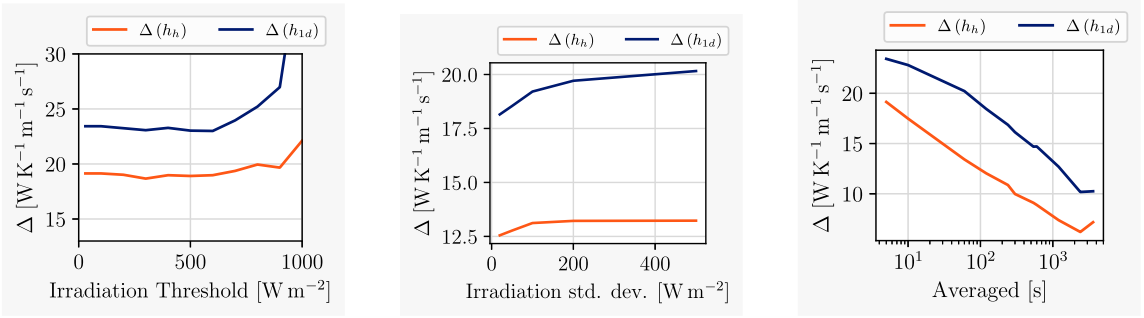

(a) Δ associated with GTI_{sw} values above thresholds.

(b) Δ associated with GTI_{sw} standard deviation below thresholds.

(c) Δ from data averaged over different time periods.

Fig. 12. Dispersion of CHTC measured by the dispersion parameter Δ for experimental data ($\Delta(h_h)$) and isothermal model ($\Delta(h_{1d})$) as a function of solar radiation and for different time filtering.

mean and standard deviation values. Fig. 12(b) shows the dispersion parameter when the data set is restricted to the standard deviation of solar radiation less than the value given on the x-axis. The lowest level is obtained under stable radiative conditions (standard deviation< 100 W m^{-2}), which shows that the heat flux sensor method produces better quality data in this state. As the standard deviation of the solar radiation increases, the dispersion indicator slightly increases for both methods. Indeed, the presence of cloudy spells leads to fluctuations of the heating source which favors observations of extreme values of the CHTC and therefore the increase in the dispersion indicator. This behavior is more pronounced for the isothermal method.

Another important parameter that drives the dispersion of the signal is time filtering, the evolution of the dispersion parameter for data filtered with a typical time range between 5 s and 1 h is shown in Fig. 12(c). As time filtering increases, the dispersion indicator decreases at the same rate as expected for the two methods. It is important to note that the two curves never cross, meaning that the isothermal model exhibits the larger dispersion parameter for any filtering time. This result is surprising as one may imagine that averaging the data over long periods of time artificially creates steady state situations, meaning that the isothermal model should be more efficient. Indeed, it is likely that the hypothesis made for the convective transfer over the rear side plays a significant role that persists when permanent conditions are mimicked. Thus, the proposed method based on the heat flux sensor is assessed to provide a more consistent CHTC estimation when compared to the traditional technique that suffers from external pollution that fundamentally biases the evaluation of the CHTC.

3.4. Simulated rear-side module temperature for urban environment

The rear surface temperature was simulated throughout the 16 days of the first measurement campaign on the laboratory solar platform using the multilayer thermal model presented in Section 2.5. Three data inputs for the CHTC were implemented and compared for the h_{fr} value: the measured value h_{h}, the median correlation of the heat flux sensor ($h_{\mathrm{h},0.5}$) and the empirical correlation of Test et al. [8] given by Eq. (1) (h_{Te}). The simulation results are presented in Fig. 13 for the 5th day of the campaign shown in Fig. 4 and for the entire period using MBE and RMSE.

The temperature time series indicates that the thermal prediction using the heat flux sensor is dramatically improved, as predicted temperatures using the heat flux sensor are close to the measured module temperature. It is important to note that convective heat transfer at the rear of the module is modeled by an empirical natural convection law. The relatively good matching between the experimental temperature and the simulated temperature tends to show that the convective heat exchange on the surface of the module is dominated by the heat exchange at the front side. Therefore, the use of natural convection on the rear side has a limited impact on temperature. This observation holds for both methods of implementation in the thermal model. The linear law $h_{\mathrm{h},0.5}$ produces a larger magnitude of errors compared to the direct implementation of the output of the heat flux sensor h_{h}. This can be explained by the fact that the linear laws do not completely reproduce the complexity of the convective mechanism. This is also suggested by the CHTC time series, which highlight the difference in magnitude and dynamics of the heat flux sensor outputs with respect to the linear law determined and the CHTC from Test et al.

A closer examination around 2 a.m. revealed that the temperature dynamics was reproduced by each method, whereas CHTCs underwent rather distinct levels of magnitude. Furthermore, the measured CHTC exhibited greater variability over short time scales compared to linear functions related to the wind. This had a notable impact on reducing the variability of temperature prediction, underlining the significant improvement achieved by using heat flux sensor methods and linear correlations derived from the use of sensor data.

This assessment performed for the 5th day of the measurement campaign is generalized and holds for the entire period, as shown in the RMSE-MBE plane to the right of the figure. Basically, empirical correlation from the literature leads to an overestimation of the rear temperature by 4 °C on average. Empirical correlation using the heat flux sensor mainly leads to correcting the bias, whereas it has little impact on the fluctuation overall. It is speculated that the remaining fluctuating error can be corrected by better accounting for the rear-side convective transfer in the thermal model and by better consideration of photoconversion at the cell level.

3.5. Front-side convective heat rates for floating photovoltaic modules

Building on the insights derived from the first measurement campaign, a parallel analysis was conducted in the second experimental setup located on a reservoir and described in Section 2.4. A new empirical correlation for the CHTC h was determined as was an empirical correlation for the global transmittance U_{values}. Additionally, we aimed to identify the restrictions of the global transmittance method when trying to understand the role of the wind in the cooling processes.

Fig. 14(a) shows a significant relationship between the CHTC calculated from the heat flux sensor methodology and the mean wind speed. The median regression reads:

$$h_{\mathrm{h},0.5} = 2.9\overline{U} + 8.97 \tag{14}$$

The wind dependency component $h_v = 2.9$ W s K^{-1} m^{-3} is higher than that recorded for the first measurement campaign (Fig. 10) but

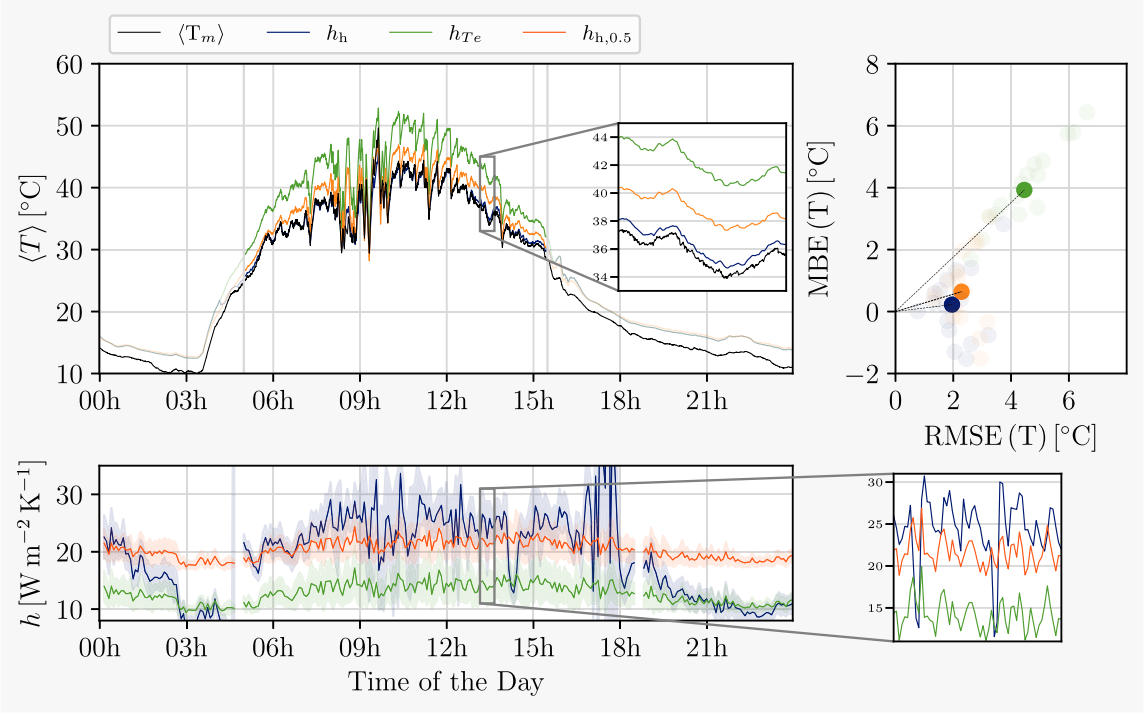

Fig. 13. **(top)** Experimental and predicted rear-side module temperature for the 5th day of the measurement campaign for different CHTC on the front-side. **(bottom)** Measured and averaged over 5 min bins, CHTC (colored background shows the standard deviations on each 5 min bin). **(right)** Performance metrics for each day (over the period depicted by the plain colored time series) of the measurement campaigns; the median values are depicted in plain colors.

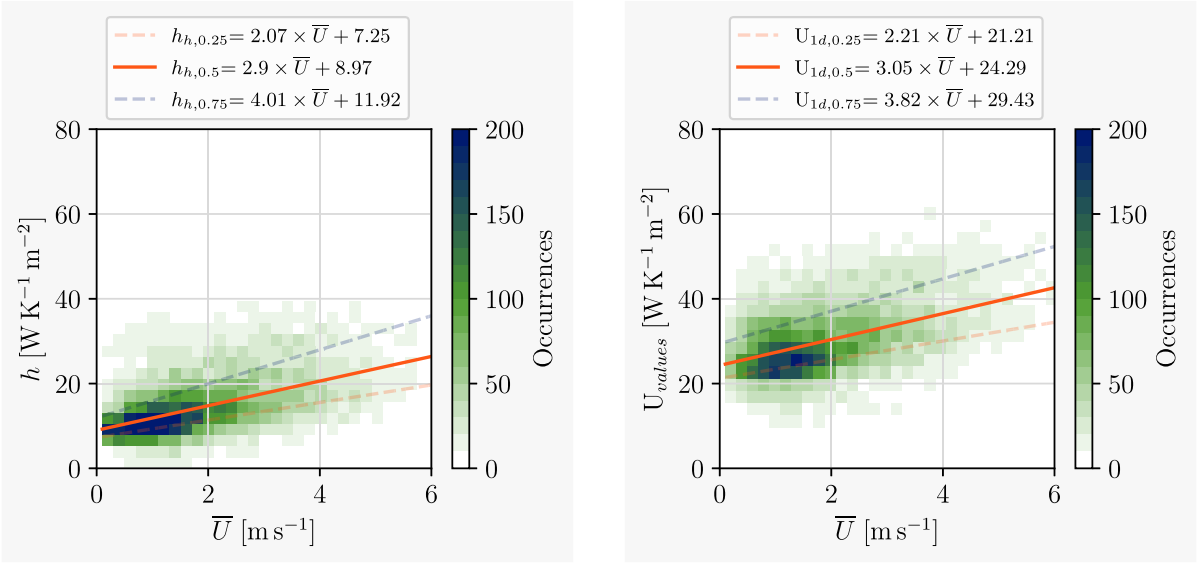

(a) *Convective heat transfer coefficient* **(b)** *Overall heat transfer coefficient*

Fig. 14. Measurements and quartile regressions of the CHTC (a) and U_{values} (b) with respect to wind velocity for FPV system. The colormap indicates the number of occurrences.

remains in a close agreement with the wind coefficient obtained by Test et al. (Eq. (1)); an increase of around 13% was observed. This difference could come from the statistical tool used to determine the linear law. Indeed, using quantile regression instead of the classical root mean square algorithm can change the correlation coefficient, as shown in Fig. 11 for the campaign of the laboratory solar platform. Furthermore, this difference could also come from geometry, since the photovoltaic module was less tilted than that used by Test et al. (30° versus 40°). It can also be speculated that the direction of the wind may have affected the level of convective cooling, as in Test et al. the plate was oriented to face the wind.

Another striking observation is the significant difference in the constant value h_c between the two measurement campaigns, which is around 8.96 W K^{-1} m^{-2}; while the difference in coefficients h_v is only 0.6 W s K^{-1} m^{-3}. The solar platform located on the roof of a 16 m high building yielded the highest value of the constant coefficient h_c. This is likely due to the highest intensity of turbulence in comparison to the FPV experiment on a lake and the correlation of Test et al. which

was designed to reduce turbulence by incorporating wind barriers near the PV module. Therefore, this result is consistent assuming that the magnitude of the constant coefficient is presumed to increase with the level of turbulence in the environment (see Sections 1 and 3.2).

In Fig. 14(b), the focus is on analyzing the global transmittance values (Eq. (6)) as a function of wind speed.

The median function reads:

$$U_{values} = 3.05\overline{U} + 24.29 \tag{15}$$

In the FPV experiment, the electrical yield was not measured (see Section 2.4) and the global transmittance was computed assuming a constant electrical power $P_{elec} = 25\,W\,m^{-2}$. Indeed, the module was connected to a battery assumed to be fully charged in the afternoon periods when data were collected to formulate Eq. (15). Therefore, the instantaneous consumption corresponded to the power of the acquisition system. Assuming a lower production level would have slightly increased U_{values} and the wind-related coefficient and vice-versa. The advantage of the heat flux sensor methods lies in its independence from knowledge of electrical production; the heat rates were determined without supplementary electrical measurements or hypotheses related to this parameter.

Moreover, U_{values} inherently incorporates the effects of thermal radiations and Eqs. (6) and (7) lead to:

$$\begin{aligned} U_{values} &= h_{fr} + h_{re} + \alpha_{lw,m,fr}\frac{\sigma T_m^4 - GTI_{lw}}{T_m - T_{amb}} + \alpha_{lw,m,re}\sigma\frac{T_m^4 - T_{amb}^4}{T_m - T_{amb}} \\ &\simeq h_{fr} + h_{re} + 4(\alpha_{lw,m,fr} + \alpha_{lw,m,re})\sigma T_m^3 \end{aligned} \tag{16}$$

where the second equation is an approximation obtained assuming that the temperature of the module is close to the ambient and sky temperatures. The first two terms on the right-hand side of Eq. (16) correspond to transmittance due to convection, whereas the last term corresponds to radiative cooling. To study this decomposition, Figs. 15(a) and 15(b) show the CHTC measured on the front side by the heat flux sensor and the global transmittance as a function of σT_m^3, respectively. The unexpected dependence of CHTC on module temperature can be explained by the correlation between module temperature and wind speed: module temperature tends to decrease with increasing wind speed. The dependence of total transmittance on module temperature is even more interesting, as it includes the radiative part of the transmittance and the dependence of temperature on wind speed. Indeed, the wind-related coefficient for the total transmittance (Fig. 15(b)) is much higher than that for the front-side CHTC (Fig. 15(a)). Therefore, as expected, the overall transmission coefficient depends on the module temperature, which is not taken into account in classical regression $U_{values}(\overline{U})$. Fig. 15(b) also shows that the dispersion is dramatically reduced for high module temperature. Indeed, for a large module temperature, the radiative part of the transmittance increases, and the global transmittance becomes highly correlated to this parameter.

Consequently, using U_{values} is appropriate to assess heat loss performance in general, but it is limited to assess specific phenomena such as forced convective action, which is more accurately described by the CHTC.

3.6. Modeling performance for floating photovoltaic modules

The CHTC values obtained from the heat flux sensor were included in the photovoltaic model to predict the rear side temperature of the floating module; these results were subsequently compared to those derived from empirical correlations for reference. Fig. 16 presents these findings for the 21st day of the measurement campaign and introduces the time series for the CHTC. As introduced in Fig. 6, this specific day is characterized by evolving conditions that lower the accuracy of empirical laws built using a quasi-permanent regime hypothesis. More precisely, a temperature increase is clearly observed between 12:00 and 13:18 as a result of the cloudy-sky to clear-sky transition shown in Figs. 6 and 7. Zooming over this time window (Fig. 16 top-left), it can be observed that the heat flux sensor inputs lead to substantial improvements in prediction. Indeed, the maximum temperature deviation, observed at the end of the temperature ramp is significantly reduced from 9.5 °C to 5.2 °C when using empirical correlations. Most of the time the CHTC value h_h is higher than that in the literature during this time window, as shown by the figures at the bottom. These larger values could indicate that the heat flux sensor captures supplementary processes responsible for the increase in the CHTCs, such as the turbulence intensity level.

These events were reproduced until 3 p.m., after which the heat transfer coefficients became comparable in magnitude. In addition, it is noteworthy that the raft motion significantly affected the spatial deviation of the experimental temperature by impacting the irradiation levels. This behavior is largely observable for clear-sky conditions during the afternoon. On the right side of Fig. 16, the statistical metrics computed for the entire period are also indicated, highlighting the superior performance for temperature prediction when using heat flux sensor data. More specifically, the median RMSE decreased to 2.62 °C compared to 4.23 °C when empirical correlations were used. A notable reduction in bias (MBE) was observed, with a decrease from 2.85 °C to 1.43 °C. Although the use of the heat flux sensor improved the prediction of the rear-side temperature compared to the implementation of a generic empirical law; statistical errors were higher than those obtained in the first measurement campaign (see Fig. 13). It is possible that the use of the temperature of the PV module in the calculation of the CHTC, instead of the heat flux sensor temperature, participated in degrading the prediction.

4. Conclusion

This study introduced a novel experimental method to improve the determination of convective heat transfer coefficients for photovoltaic applications. The method is based on two central elements: the use of a heat flux sensor and statistical treatments using quantile regression. The heat flux sensor is placed on top of the PV module surface so that the methodology can be easily deployed in existing applications.

Convective laws were produced with a higher level of confidence because the method significantly reduced the measurement and statistical errors that pollute the traditional method of determination. The method proposed significantly reduces the dispersion of CHTC records without modifying PV operating conditions. Importantly, quantile regression was found to provide a practical tool that provides better understanding of the complex relationship between the PV system and its environment. We strongly suggest that this statistical tool be utilized for future PV thermal assessments, as it reduces the influence of outlier records and allows quantifying any potential dependence of the observed variable (i.e., CHTC) dispersion on the explanatory variable (i.e., mean wind velocity).

The method proposed has the advantage of calculating the front-side CHTC, unlike traditional CHTC values that are usually based on the energy balance at the PV module level. Therefore, the direct heat flux measurement presented in this study does not require knowledge of the CHTC at the rear side of the module, which remains a specific challenge as the airflow behind the PV modules is poorly known. Therefore, the direct determination of CHTC allowed us to improve temperature predictions by around 2 K. Moreover, the methodology proposed can be applied to investigate the heat transfer at the rear side. Furthermore, determining the appropriate CHTC for a real solar power plant is typically challenging since the conventional approach based on a global transmittance value U_{values} requires power generation data, which are often not available at the PV module level. Given that silicon solar cells exhibit a temperature coefficient of approximately 0.4 %/K for power ratings, using heat flux sensors to measure local CHTC could improve PV electrical prediction by at least 0.8 %.

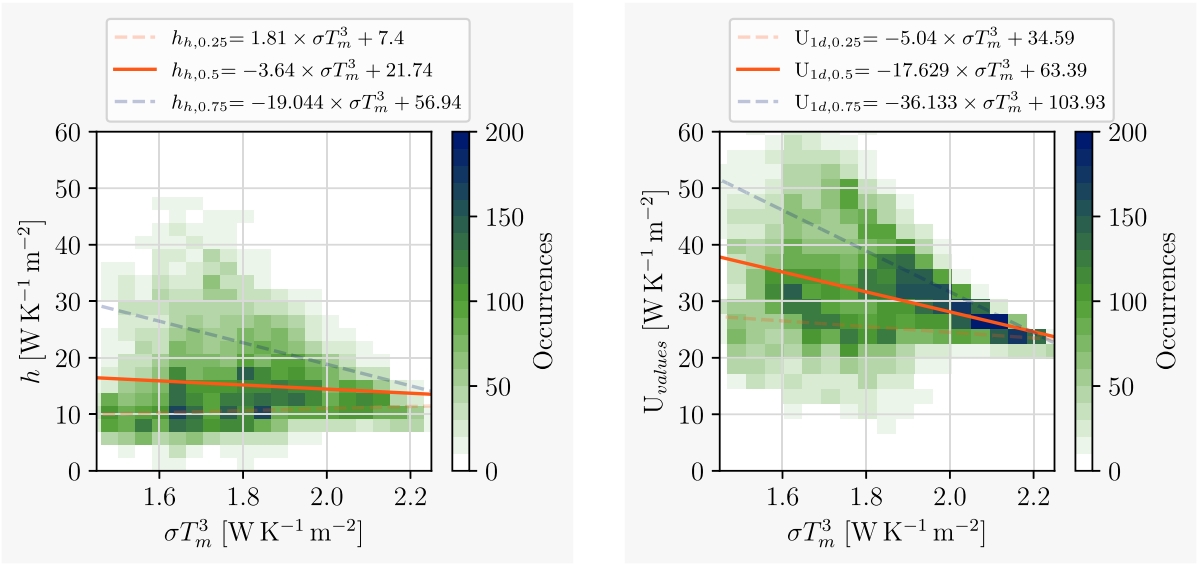

(a) h_h *from heat flux sensor.* **(b)** U_{values} *from module energy balance.*

Fig. 15. Distribution of the convective heat losses h_h (a) and global heat losses U_{values} (b), with respect to module temperature. Quantile regressions for $\tau = 0.25$, $\tau = 0.5$ and $\tau = 0.75$ are indicated.

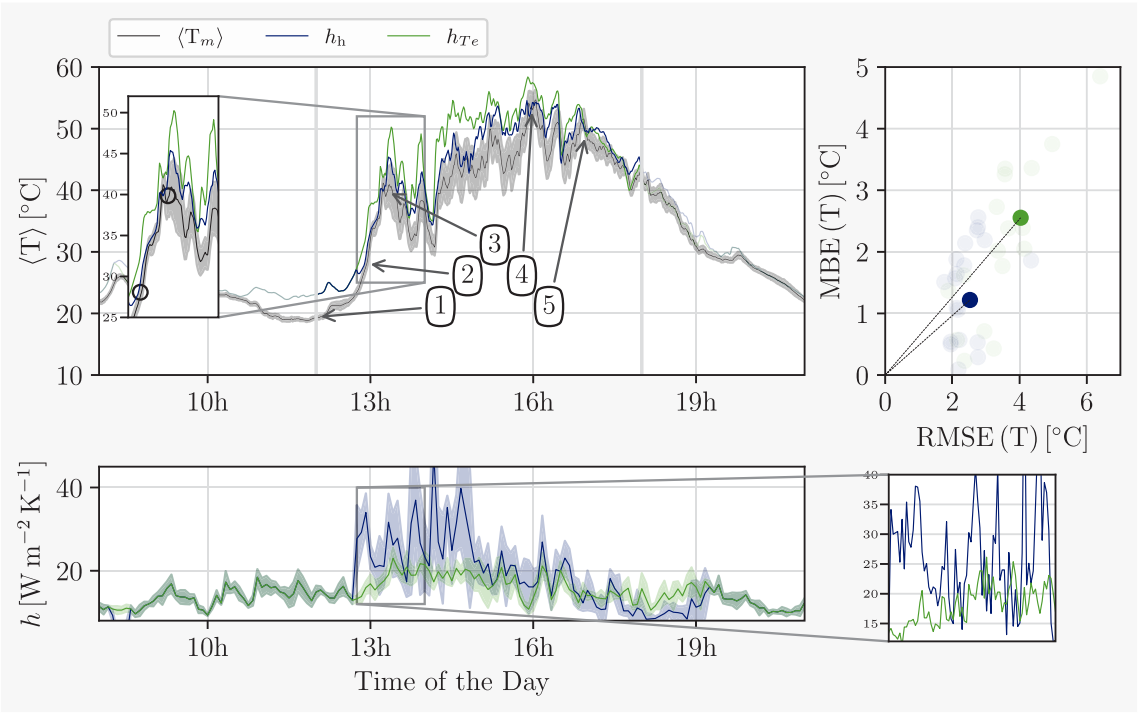

Fig. 16. **(top)** Comparison of experimental module temperature measured at the rear side $\langle T_m \rangle$ versus temperature predictions using different CHTCs on the front-side: experimental CHTC ($T_{re}(h_h)$) and empirical law from [8] ($T_{re}(h_{Te})$). Annotated numbers indicate the camera snapshot of Fig. 7. **(right)** Statistical performances are computed over the period depicted by plain colored time series. **(bottom)** CHTC averaged over 5 min for the heat flux sensor and the empirical correlation. Colored background depicts standard deviations over each 5 min bin.

Using this methodology, a new correlation for convective heat transfer coefficient adapted to a FPV setup was derived, i.e. $h_h = 2.9\overline{U} + 8.97$ (W K^{-1} m^{-2}). It is slightly more sensitive to wind velocity than the correlation in the literature based on a similar PV module geometry and distribution of environmental probes. Given that a standalone FPV module was monitored in the study, the reader may find different sets of coefficients for large-scale solar arrays with other installation footprints. We recommend applying the correlation provided for a floating configuration with large spacings. More importantly, implementing the determined CHTC in the energy yield assessment tool showed that the rear side temperature was accurately reproduced, signifying that convective mechanisms are likely to be responsible of the cooling effect on floating photovoltaic applications. Thus, we suggest that the effort to develop FPV thermal model should focus on the accurate description of convective processes to model the *cooling effect*.

The methodology proposed has the potential to improve the thermal management of PV assets because it relies only on environmental data and achieves higher monitoring rates without influencing PV operating

conditions. More research must be performed to evaluate the extent to which cell covering is possible, in order to position the probe at different locations of the module so that accurate local CHTCs can be captured for large size installations. This method also offers the opportunity to investigate the convective heat transfer over the rear module surface for which there is no accepted correlation as the latter depends on geometric and environmental conditions. Finally, the methodology proposed can be used to investigate the role of wind directions and turbulence effects in outdoor environments. They probably represent the next frontiers to cross for improving the thermal management of PV modules.

CRediT authorship contribution statement

Baptiste Amiot: Conceptualization, Data curation, Formal analysis, Investigation, Methodology, Software, Validation, Visualization, Writing – original draft, Writing – review & editing. **Hervé Pabiou:** Conceptualization, Formal analysis, Investigation, Methodology, Resources, Supervision, Validation, Writing – original draft, Writing – review & editing. **Rémi Le Berre:** Funding acquisition, Project administration, Resources, Supervision. **Stéphanie Giroux–Julien:** Funding acquisition, Methodology, Project administration, Resources, Supervision, Writing – review & editing.

Declaration of competing interest

The authors declare that they have no known competing financial interests or personal relationships that could have appeared to influence the work reported in this paper.

Acknowledgments

This research was carried out as part of the first author's PhD studies (ANRT/EDF-CIFRE Grant/Award number: 2019/1278). The authors also thank Dr. Agnès Delmas (CETHIL) and Dr. Fabien Mandorlo (Institut de Nanotechnologie de Lyon) for the spectrometry measurements, Gaëtan Bayart and Jonhatan Delatre (EDF Renouvelables) for access to the reservoir, Benoit Gire, Gilles Derail and Dr. Antoine Thouvenot (ATHOS environnement) for field work on the floating raft. We finally express our sincere gratitude to the reviewers whose insightful comments and constructive feedback have significantly contributed to improving the quality and clarity of this paper.

Appendix A

A.1. Convective heat transfer relationship with wind velocity

Indeed, the transfer of heat over a PV panel is similar to the academic configuration of forced convection over a flat plate which is extensively covered in textbooks [41]. In dimensionless form, heat transfer is analyzed in terms of Reynolds number $Re = \overline{U}L/\nu$, Prandtl number $Pr = \nu/\kappa$ and Nusselt number $Nu = hL/k$ where $\overline{U}$ is the incoming velocity, L is the typical length of the system, ν and k are the kinematic viscosity and the thermal conductivity of the fluid, respectively. As air is the only fluid encountered in PV applications, the Prandtl number can be considered as a constant and the Reynolds and Nusselt numbers follow a power-law: $Nu = aRe^b$ where a and b are constants. In outdoor conditions, a $\overline{U}_0 = 1\,\mathrm{m\,s^{-1}}$ wind speed over a $L_0 = 1$ m-long solar panel results in a Reynolds number around $Re_0 = 10^5$ which means that airflow is mostly turbulent above PV panels. For turbulent forced convection, b is in the range $[0.8 - 1]$ and such power-laws are valid for several decades of Reynolds number, whereas in the specific case of heat transfer over a PV module, the typical length and velocity ranges fall within the ranges $[1 - 2]$m and $[0.5 - 8]\mathrm{ms}^{-1}$, respectively. Thus, the Reynolds number varies over one decade and the power-law can be linearized with a limited loss of accuracy:

$$Nu = Nu(Re_0) + abRe_0^{b-1}(Re - Re_0) \tag{A.1}$$

where Re_0 is a typical value of the Reynolds number for the system. It is important to note that such a relationship has a limited range of validity depending on the experimental (or numerical) data set. In particular, the constant term in Eq. (A.1) can be seen as the typical value of the Nusselt number in the selected range of the Reynolds number, whereas the other term shows dependence on the Reynolds number. Returning to the dimensional variables, Eq. (A.1) reads:

$$h = h_c + h_v\overline{U} \tag{A.2}$$

where h_v is the wind dependency component given in $\mathrm{W\,s\,K^{-1}\,m^{-3}}$ and h_c is a constant. It is important to note that h_c cannot be interpreted as the CHTC at zero velocity, since Eq. (A.1) is only valid for forced convection.

A.2. Calculation of net radiative heat flux leaving the sensor

The net radiative heat flux leaving the heat flux sensor ϕ_{rad} is given by:

$$\phi_{rad} = \epsilon\sigma T_\mathrm{h}^4 - \alpha_{sw,\mathrm{h}}\mathrm{GTI}_{sw} - \alpha_{lw,\mathrm{h}}\mathrm{GTI}_{lw} \tag{A.3}$$

where $\sigma = 5.67 \times 10^{-8}\,\mathrm{W\,m^{-2}\,K^{-4}}$ is the Stefan–Boltzmann constant, T_h is the temperature of the sensor, GTI_{sw} and GTI_{lw} are the incoming radiation in the plane of the module in the short and long wavelength ranges, respectively. ϵ is the total, hemispherical emissivity of the sensor, $\alpha_{sw,\mathrm{h}}$ and $\alpha_{lw,\mathrm{h}}$ are the absorptivities of the sensor in the short and long wavelength ranges, respectively. The cut-off wavelength is usually chosen to be equal to 3 μm.

In this study, the spectral normal emissivity of the coatings of the sensor is measured by an integrated sphere mounted in a Fourier Transform Spectrometer and the global tilted irradiations GTI_{sw} and GTI_{sw} are measured by a pyranometer and a pyrgeometer, respectively.

To calculate the radiative properties used in Eq. (A.3) the surface of the sensor is assumed to be gray over the short and long wave ranges. Therefore, the total normal emissivity ($\epsilon^{\perp}_{sw}$, $\epsilon^{\perp}_{lw}$) on each band is calculated by averaging the spectral normal emissivity ($\epsilon^{\perp}_{sw,\lambda}, \epsilon^{\perp}_{lw,\lambda}$) measured by the integrating sphere. Then, the surface is assumed to be isotropic in emission and absorption. Under this assumption, the total normal emissivity is equal to the total hemispherical emissivity ($\epsilon^{\cap}_{sw}$, $\epsilon^{\cap}_{lw}$) on each band:

$$\epsilon^{\cap}_{sw} = \epsilon^{\perp}_{sw} = \frac{1}{\lambda_2 - \lambda_1}\int_{\lambda_1}^{\lambda_2}\epsilon^{\perp}_{sw,\lambda}\,d\lambda \tag{A.4}$$

$$\epsilon^{\cap}_{lw} = \epsilon^{\perp}_{lw} = \frac{1}{\lambda_4 - \lambda_3}\int_{\lambda_3}^{\lambda_4}\epsilon^{\perp}_{sw,\lambda}\,d\lambda \tag{A.5}$$

Under the assumption of gray and isotropic (in emission and absorption) surface on each spectral band, Kirchoff's law leads to:

$$\alpha_{sw,\mathrm{h}} = \epsilon^{\cap}_{sw} \tag{A.6}$$

$$\alpha_{lw,\mathrm{h}} = \epsilon^{\cap}_{lw} \tag{A.7}$$

From these two quantities, the total emissivity on the whole spectrum of the surface is given by:

$$\epsilon = F(\lambda^* T_\mathrm{h})\alpha_{sw,\mathrm{h}} + (1 - F(\lambda^* T_\mathrm{h}))\alpha_{lw,\mathrm{h}} \tag{A.8}$$

where $\lambda^* = 3$ μm is the cut-off wavelength between the short and long wavelength ranges, T_h is the temperature of the sensor and $F(\lambda^* T_\mathrm{h})$ is the fractional blackbody emissive power which defined by:

$$F(\lambda^* T_\mathrm{h}) = \frac{1}{\sigma T_\mathrm{h}^4}\int_0^{\lambda^*} E^0(\lambda, T)\,d\lambda \tag{A.9}$$

where $\sigma = 6.67 \times 10^{-8}\,\mathrm{Wm^{-2}K^{-1}}$ is the Stefan–Boltzmann constant and $E^0(\lambda, T)$ is the blackbody emissive power. As the temperature of the

Table A.6
Radiative properties of the coatings applied on different materials and obtained from the laboratory spectroscopy measurements.

	White painting	Black painting
$\alpha_{sw,\mathrm{h}}$	0,30	0,95
$\epsilon = \alpha_{lw,\mathrm{h}}$	0,51	0,95

heat flux sensor remains below 100 °C, the first term in Eq. (A.8) is negligible and the total emissivity of the surface is approximated to within 1% by the emissivity in the long wavelength range:

$$\epsilon = \alpha_{lw,\mathrm{h}} \tag{A.10}$$

The values of these radiative properties are shown in Table A.6 for the white and black paintings.

Finally, to calculate the net radiative heat flux leaving the sensor (Eq. (A.3)), the incoming radiation in the short and long wavelength ranges are obtained by the pyranometer and the pyrgeometer, respectively.

References

[1] D. Evans, Simplified method for predicting photovoltaic array output, Sol. Energy 27 (6) (1981) 555–560, http://dx.doi.org/10.1016/0038-092X(81)90051-7, URL https://linkinghub.elsevier.com/retrieve/pii/0038092X81900517.

[2] E. Skoplaki, J.A. Palyvos, Operating temperature of photovoltaic modules: A survey of pertinent correlations, Renew. Energy 34 (1) (2009) 23–29, http://dx.doi.org/10.1016/j.renene.2008.04.009.

[3] M. Theristis, N. Riedel-Lyngskær, J.S. Stein, L. Deville, L. Micheli, A. Driesse, W.B. Hobbs, S. Ovaitt, R. Daxini, D. Barrie, M. Campanelli, H. Hodges, J.R. Ledesma, I. Lokhat, B. McCormick, B. Meng, B. Miller, R. Motta, E. Noirault, M. Parker, J. Polo, D. Powell, R. Moretón, M. Prilliman, S. Ransome, M. Schneider, B. Schnierer, B. Tian, F. Warner, R. Williams, B. Wittmer, C. Zhao, Blind photovoltaic modeling intercomparison: A multidimensional data analysis and lessons learned, Prog. Photovolt., Res. Appl. (2023) http://dx.doi.org/10.1002/pip.3729.

[4] A. Driesse, J. Stein, M. Theristis, Improving common PV module temperature models by incorporating radiative losses to the sky, Office of Scientific and Technical Information (OSTI), 2022, http://dx.doi.org/10.2172/1884890.

[5] E.M. Sparrow, S.C. Lau, Effect of adiabatic co-planar extension surfaces on wind-related solar-collector heat transfer coefficients, J. Heat Transfer 103 (2) (1981) 268–271, http://dx.doi.org/10.1115/1.3244452.

[6] R.J. Kind, D.H. Gladstone, A.D. Moizer, Convective heat losses from flat-plate solar collectors in turbulent winds, J. Sol. Energy Eng. 105 (1) (1983) 80–85, http://dx.doi.org/10.1115/1.3266350.

[7] S. Sharples, P. Charlesworth, Full-scale measurements of wind-induced convective heat transfer from a roof-mounted flat plate solar collector, Sol. Energy 62 (2) (1998) 69–77, http://dx.doi.org/10.1016/s0038-092x(97)00119-9.

[8] F.L. Test, R.C. Lessmann, A. Johary, Heat transfer during wind flow ower rectangular bodies in the natural environment, J. Heat Transfer 103 (2) (1981) 262–267, http://dx.doi.org/10.1115/1.3244451.

[9] S. Kumar, S.C. Mullick, Wind heat transfer coefficient in solar collectors in outdoor conditions, Sol. Energy 84 (6) (2010) 956–963, http://dx.doi.org/10.1016/j.solener.2010.03.003.

[10] S. Armstrong, W.G. Hurley, A thermal model for photovoltaic panels under varying atmospheric conditions, Appl. Therm. Eng. 30 (11–12) (2010) 1488–1495, http://dx.doi.org/10.1016/j.applthermaleng.2010.03.012.

[11] S. Sharples, P.S. Charlesworth, Full-scale measurements of wind-induced convective heat transfer from a roof-mounted flat plate solar collector, Sol. Energy 62 (2) (1998) 69–77.

[12] N. Bishara, G. Pernigotto, A. Prada, M. Baratieri, A. Gasparella, Experimental determination of the building envelope's dynamic thermal characteristics in consideration of hygrothermal modelling – Assessment of methods and sources of uncertainty, Energy Build. 236 (110798) (2021) http://dx.doi.org/10.1016/j.enbuild.2021.110798.

[13] M. Cucumo, V. Ferraro, D. Kaliakatsos, M. Mele, On the distortion of thermal flux and of surface temperature induced by heat flux sensors positioned on the inner surface of buildings, Energy Build. 158 (2018) 677–683, http://dx.doi.org/10.1016/j.enbuild.2017.10.034.

[14] L. Evangelisti, C. Guattari, R.D.L. Vollaro, F. Asdrubali, A methodological approach for heat-flow meter data post-processing under different climatic conditions and wall orientations, Energy Build. 223 (2020) 110216, http://dx.doi.org/10.1016/j.enbuild.2020.110216.

[15] R. Albatici, A.M. Tonelli, M. Chiogna, A comprehensive experimental approach for the validation of quantitative infrared thermography in the evaluation of building thermal transmittance, Appl. Energy 141 (2015) 218–228, http://dx.doi.org/10.1016/j.apenergy.2014.12.035.

[16] Y. Hayakawa, D. Sato, N. Yamada, Measurement of the convective heat transfer coefficient and temperature of vehicle-integrated photovoltaic modules, Energies 15 (13) (2022) 4818, http://dx.doi.org/10.3390/en15134818.

[17] R.M. Almeida, R. Schmitt, S.M. Grodsky, A.S. Flecker, C.P. Gomes, L. Zhao, H. Liu, N. Barros, R. Kelman, P.B. McIntyre, Floating solar power could help fight climate change — let's get it right, Nature 606 (7913) (2022) 246–249, http://dx.doi.org/10.1038/d41586-022-01525-1.

[18] G. Exley, A. Armstrong, T. Page, I.D. Jones, Floating photovoltaics could mitigate climate change impacts on water body temperature and stratification, Sol. Energy 219 (2021) 24–33, http://dx.doi.org/10.1016/j.solener.2021.01.076, Special Issue on Floating Solar: beyond the state of the art technology URL https://www.sciencedirect.com/science/article/pii/S0038092X2100116X.

[19] R. Nobre, S.M. Rocha, S. Healing, Q. Ji, S. Boulêtreau, A. Armstrong, J. Cucherousset, A global study of freshwater coverage by floating photovoltaics, Sol. Energy 267 (2024) 112244, http://dx.doi.org/10.1016/j.solener.2023.112244, URL https://www.sciencedirect.com/science/article/pii/S0038092X23008782.

[20] L. Micheli, D.L. Talavera, G. Marco Tina, F. Almonacid, E.F. Fernández, Techno-economic potential and perspectives of floating photovoltaics in europe, Sol. Energy 243 (2022) 203–214, http://dx.doi.org/10.1016/j.solener.2022.07.042.

[21] G.M. Tina, F.B. Scavo, L. Merlo, F. Bizzarri, Analysis of water environment on the production of floating photovoltaic plants, Renew. Energy 175 (2021) 281–295, http://dx.doi.org/10.1016/j.renene.2021.04.082.

[22] P. Li, X. Gao, Z. Li, T. Ye, X. Zhou, Effects of fishery complementary photovoltaic power plant on radiation, energy flux and driving forces under different synoptic conditions, Sci. Rep. 13 (1) (2023) http://dx.doi.org/10.1038/s41598-023-36314-x.

[23] S. Assouline, K. Narkis, D. Or, Evaporation from partially covered water surfaces, Water Resour. Res. 46 (10) (2010) http://dx.doi.org/10.1029/2010wr009121.

[24] H. Liu, V. Krishna, J. Lun Leung, T. Reindl, L. Zhao, Field experience and performance analysis of floating PV technologies in the tropics, Prog. Photovolt., Res. Appl. 26 (12) (2018) 957–967, http://dx.doi.org/10.1002/pip.3039, URL http://doi.wiley.com/10.1002/pip.3039.

[25] F. Bontempo Scavo, G.M. Tina, A. Gagliano, S. Nižetić, An assessment study of evaporation rate models on a water basin with floating photovoltaic plants, Int. J. Energy Res. 45 (1) (2021) 167–188, http://dx.doi.org/10.1002/er.5170, URL https://onlinelibrary.wiley.com/doi/10.1002/er.5170.

[26] I. Peters, A. Nobre, Deciphering the thermal behavior of floating photovoltaic installations, Sol. Energy Adv. 2 (November 2021) (2022) 100007, http://dx.doi.org/10.1016/j.seja.2021.100007.

[27] M. Dörenkämper, A. Wahed, A. Kumar, M. de Jong, J. Kroon, T. Reindl, The cooling effect of floating PV in two different climate zones: A comparison of field test data from the netherlands and Singapore, Sol. Energy 214 (December 2020) (2021) 239–247, http://dx.doi.org/10.1016/j.solener.2020.11.029.

[28] A. Glick, N. Ali, J. Bossuyt, M. Calaf, R.B. Cal, Utility-scale solar PV performance enhancements through system-level modifications, Sci. Rep. 10 (1) (2020) 1–9, http://dx.doi.org/10.1038/s41598-020-66347-5.

[29] S.E. Smith, B. Viggiano, N. Ali, T.J. Silverman, M. Obligado, M. Calaf, R.B. Cal, Increased panel height enhances cooling for photovoltaic solar farms, Appl. Energy 325 (2022) 119819, http://dx.doi.org/10.1016/j.apenergy.2022.119819.

[30] B.J. Stanislawski, T. Harman, T.J. Silverman, R.B. Cal, M. Calaf, Row spacing as a controller of solar module temperature and power output in solar farms, J. Renew. Sustain. Energy 14 (6) (2022) 063702, http://dx.doi.org/10.1063/5.0123641, arXiv:https://pubs.aip.org/aip/jrse/article-pdf/doi/10.1063/5.0123641/16592541/063702_1_online.pdf.

[31] A. Glick, S.E. Smith, N. Ali, J. Bossuyt, G. Recktenwald, M. Calaf, R.B. Cal, Influence of flow direction and turbulence intensity on heat transfer of utility-scale photovoltaic solar farms, Sol. Energy 207 (November 2019) (2020) 173–182, http://dx.doi.org/10.1016/j.solener.2020.05.061.

[32] S.E. Smith, B.J. Stanislawski, B.K. Eng, N. Ali, T.J. Silverman, M. Calaf, R.B. Cal, Viewing convection as a solar farm phenomenon broadens modern power predictions for solar photovoltaics, J. Renew. Sustain. Energy (2022) URL https://api.semanticscholar.org/CorpusID:254357312.

[33] R. Koenker, Inference for quantile regression, Quantile Regression, Cambridge University Press, pp. 1–336, http://dx.doi.org/10.1017/cbo9780511754098.004.

[34] K. Yu, Z. Lu, J. Stander, Quantile regression: applications and current research areas, J. R. Stat. Soc: Ser. D (the Statistician) 52 (3) (2003) 331–350, http://dx.doi.org/10.1111/1467-9884.00363.

[35] S. Seabold, J. Perktold, Statsmodels: Econometric and statistical modeling with python, in: 9th Python in Science Conference, 2010, pp. 92–96.

[36] A. Pavgi, Temperature coefficients and thermal uniformity mapping of PV modules and plants, 2017, URL https://api.semanticscholar.org/CorpusID:114631724.

[37] D. Faiman, Assessing the outdoor operating temperature of photovoltaic modules, Prog. Photovolt., Res. Appl. 16 (4) (2008) 307–315, http://dx.doi.org/10.1002/pip.813.

[38] S.W. Churchill, H.H. Chu, Correlating equations for laminar and turbulent free convection from a vertical plate, Int. J. Heat Mass Transfer 18 (11) (1975) 1323–1329, http://dx.doi.org/10.1016/0017-9310(75)90243-4, URL https://linkinghub.elsevier.com/retrieve/pii/0017931075902434.

[39] J. Brkic, M. Ceran, M. Elmoghazy, R. Kavlak, A. Haumer, C. Kral, Open source PhotoVoltaics library for systemic investigations, in: LinkÖping Electronic Conference Proceedings, Linköing University Electronic Press, 2019, pp. 40–50, http://dx.doi.org/10.3384/ecp1915741.

[40] L. Weiss, M. Amara, C. Ménézo, Impact of radiative-heat transfer on photovoltaic module temperature, Prog. Photovolt: Res. Appl. 24 (2016) 12–27, http://dx.doi.org/10.1002/pip.2633.

[41] T.L. Bergman, F.P. Incropera, D.P. DeWitt, A.S. Lavine, Fundamentals of heat and mass transfer, seventh ed., John Wiley & Sons, 2011.